國立交通大學

光電工程學系
光電工程研究所

碩士論文

利用侷域性表面電漿達成高增益穿透於脊型奈米孔洞之研究

Transmission Enhancement of Ridge-based Nano Aperture by Localized Surface Plasmon

研究生：尹世瑋
指導教授：田仲豪 博士

中華民國九十六年七月

利用侷域性表面電漿達成高增益穿透於脊型奈米孔洞之研究

Transmission Enhancement of Ridge-based Nano Aperture by Localized Surface Plasmon

研 究 生: 尹世瑋　　Student: Shr-Wei Yin

指導教授: 田仲豪　　Advisor: Dr. Chung-Hao Tien

國立交通大學 電機學院

光電工程學系

光電工程研究所

碩士論文

A Thesis

Submitted to Institute of Electro-Optical Engineering &
Photonic Department
College of Electrical Engineering Science
National Chiao-Tung University
in Partial Fulfillment of the Requirements
for the Degree of Master
In
Institute of Electro-Optical Engineering

July 2007

Hsin-Chu, Taiwan, Republic of China.

中華民國九十六年七月

利用侷域性表面電漿達成高增益穿透於脊型奈米孔洞之研究

研究生：尹世瑋　　指導教授：田仲豪 博士

國立交通大學
光電工程學系 光電工程研究所

摘要

近年來，金屬次波長孔洞的光穿透異常增強的現象引起了廣大的注意以及討論，此一現象隨後以表面電漿(Surface Plasmon)的機制加以解釋，其中研究包括1998年起由T.W. Ebbesen 教授團隊所提出一系列關於金屬次波長孔洞陣列、單一金屬次波長孔洞、週期性溝槽式結構等實驗。隨後於2004年，L. Hessenlink 教授團隊所發表特殊C型孔洞應用於近場超解析光點(λ/10)，不僅具備超越繞射極限的光點，同時若與可得到相同光點大小的傳統次波長孔洞(如圓型、方型)，其光學穿透增益量可達10^3倍。同期間，M. Mansuripur也以二維有限時域差分法(FDTD)數值地分析狹縫的光增益以及光場分佈情形。

本篇論文主要目的為針對可見光波段(紅光 λ=633 nm)對次波長奈米金屬孔洞做三維模擬分析與研究，將已發表的一些特殊形狀孔洞研究作關聯性的研究，並從其相關性發展出一個複合式結構，同時達到高光穿透率以及超解析光點(~$0.2x0.2\lambda^2$)，藉以期應用在許多方面如光儲存超解析光點。

Transmission Enhancement of Ridge-based Nano Aperture by Localized Surface Plasmon

Student: Shr-Wei Yin **Advisor: Dr. Chung-Hao Tien**

Department of Photonics & Institute of Electro-Optical Engineering
National Chiao Tung University

Abstract

In recent years, the studies about extraordinary transmission through subwavelength metallic aperture have drawn more attention, called surface plasmon. These researches included subwavelength metallic hole array, single subwavelength metallic aperture, and an aperture with periodic corrugations array by T.W. Ebbesen et *al*.. As in 2004, L. Hessenlink et *al*. designed C-shaped aperture with not only spot size to $\lambda/10$ but the power throughput enhancement can achieve to ~10^3. Meanwhile, M. Mansuripur et *al*. used FDTD method to simulate the enhancement and field distributions in 2-D slit aperture.

This thesis aims to analyze the subwavelength metallic aperture in visible range (especially at λ=633 nm), and the connection of the special apertures. Base on the phenomena we observed, try to give a composite structure which could take both advantages of high transmission and small spot. The researches might be applied in super resolution spot in optical data storage system.

致謝

「因為需要感謝的人太多了，就感謝天罷」，年少懵懂時，總以為這句話代表的僅僅是考卷上的分數而已。

何其榮幸，碩士班兩年期間，能夠接受田仲豪老師在研究上，無私且細心的指導。除此之外，老師對於學生發自內心的關懷，也讓我深深的覺得溫暖，感謝之外，只有更多的感謝。

在實驗室的日子裡，最先要感謝的就是始終給予我最大支持的璧如學姊，總是不吝在專業上給予想法與協助。私底下就像一個大姊姊，在情緒低落的時候能夠開導我，開心的時候也能與一起分享。同時，也要感謝小陸，你總是在球場讓我找回信心。健翔，我會記得在你帥氣臉龐的背後，多的是天真爛漫，還有永遠唱不完的經典卡通歌曲。進哥，很遺憾我還是不知道你褲襠裡到底藏著什麼，你去打擊練習場真的都帶自己的大棒子嗎？藍藍翔，對於研究的熱忱時常讓我永遠自覺不如，從你身上我學到了，學海無崖，回頭是岸。姚哥跟 dudu，在這互相扶持的過程裡，所建立的革命情誼，比什麼都更值得珍惜。

也要特別謝謝學弟們，bug、貢丸、小潘、囂張、柏起、小余、如果實驗室的生活少了你們，我想那過程會是十分乏味的。

感謝實驗室的大家，使得原本可能枯燥沉悶的研究生生活，變的有趣而且幸福。謝謝你們，你們成就了我。

最後，我要特別謝謝妳，如果沒有妳的體諒、包容、陪伴，還有生活上的細心照顧與關懷，使我能夠無後顧之憂的研究與學習，就不會有今日的我。

「因為需要感謝的人太多了，就感謝天罷」，但願此刻的我，能夠體認這句話的意義。

Table of Contents

Figure Caption

Table Caption

Chapter 1 Introduction

1.1 Motivation

As the coming of the tera-era, the demand of the recording capacity is increasing. The capacity is governed by the spot size of the optical system. The spot correlates closely with numerical aperture (NA) and the wavelength of incidence (λ) of the optical data storage system. An optical data storage (ODS) system is developed toward a shorter wavelength laser diode and a higher numerical aperture objective lens, where the focused spot diameter is proportional to λ/NA, to achieve a higher spot density, as shown in Fig.1.1-1.

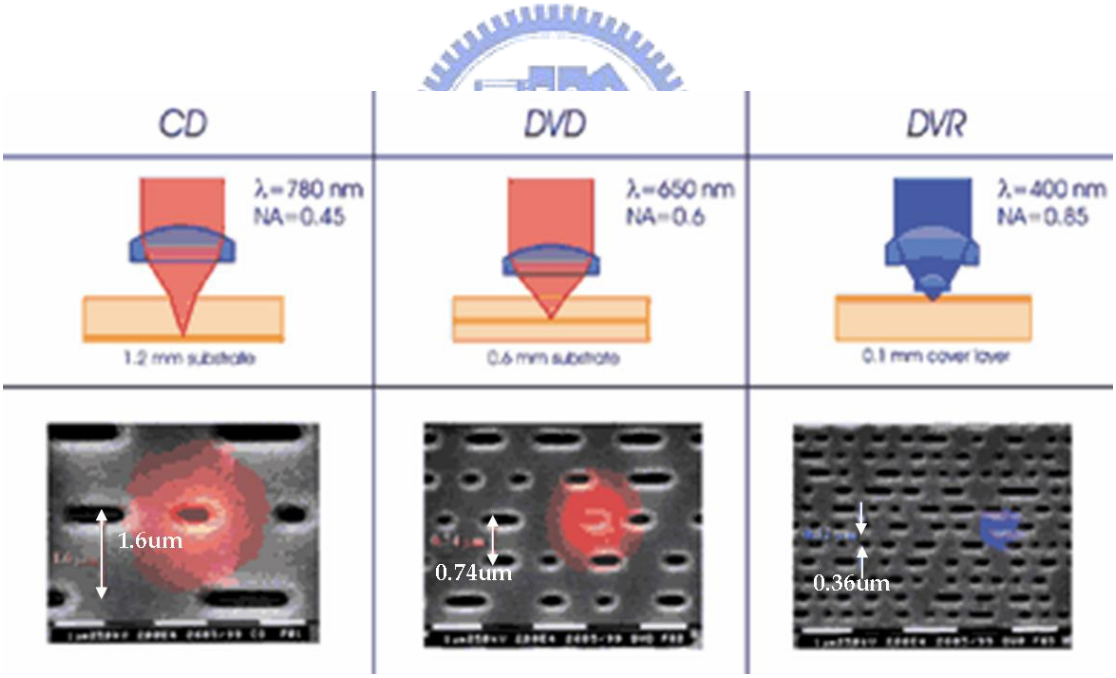

Fig. 1.1-1 Evolution of the CD, DVD and DVR system and electron microscope photographs of the information pits of the three systems.

However, the far-field diffraction also limits the spot size and recoding density accordingly. In order to get beyond the diffraction limit, the near-field

technology has drawn more attention. We would obtain the smaller spot near the light exit plane (about $0.05\lambda^2$ nm^2) while light transmit through the sub-wavelength (nano scale) metallic aperture. Fig.1.1-2. shows some fabrication of sub-wavelength aperture.

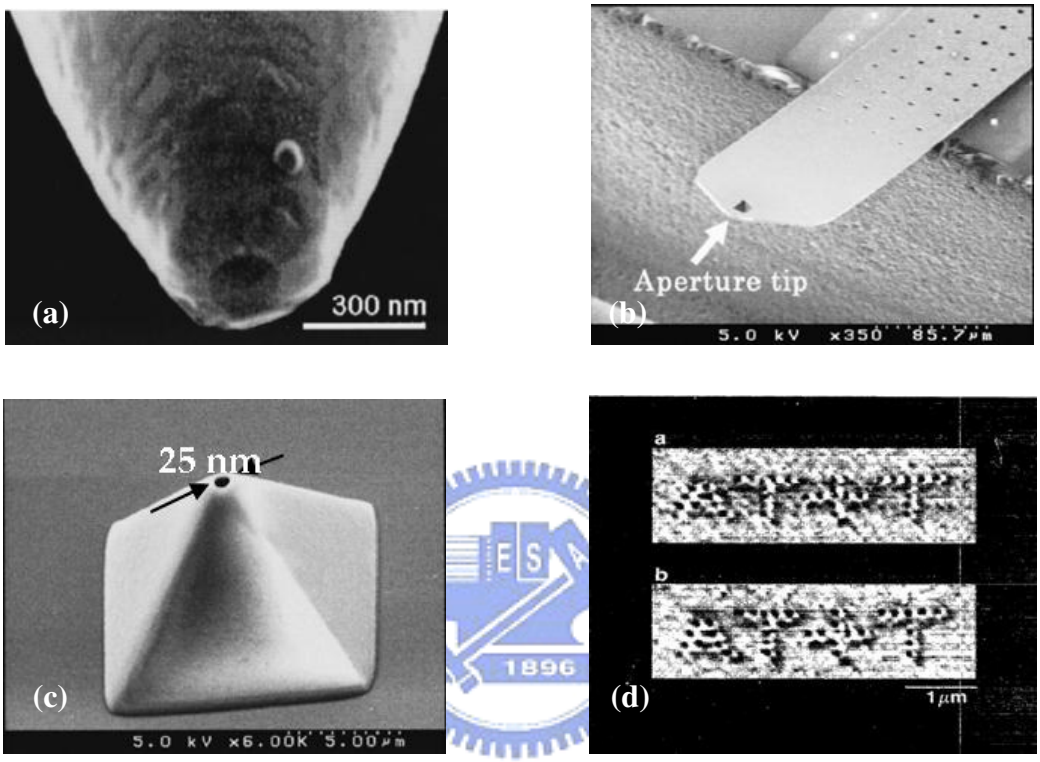

Fig. 1.1-2 (a), (b) and (c) are fabrication of sub-wavelength aperture, (d) is the spot overcome diffraction limit at near-field observation.

Unfortunately, according to fundamental waveguide theory, when the aperture width is under a half of wavelength of incidence, the fundamental propagation mode could not be sustained inside the aperture. The light throughput will be very low (PT=$1.33*10^{-2}$ when spot size was kept in $0.04\lambda^2$ nm^2 for λ=633 nm in square aperture 60*60 nm^2) to influence the reading/writing efficiency of ODS system. How to enhance the light transmission under the sub-wavelength aperture has gathered great importance in recent years.

1.2 Objectives

Based on the Bethe's theory, localized surface plasmon (LSP) effect, and aperture reforming, we analyzed the optical properties of light transmission through the metallic nano aperture and declare the mechanism of special apertures with great high transmission. The objectives of this thesis are to propose a novel aperture to enhance the light transmission without loss of spatial resolution.

1.3 Organization

The objective of the thesis is to design a novel nano-aperture that can provide adequate transmittance for practicability

This thesis is organized to review the basic principles and the literatures utilized to build the model and establish basic knowledge in Chapter 2. We proposed to understand the extraordinary light transmission mechanism first. Simulation model and results are described in Chapter 3, followed by designing the composite structure will be implemented to make the comparison to the traditional subwavelength aperture. Finally we summarize the thesis and future work in Chapter 4.

Chapter 2 Theory and Literature Review

The most primary research to the light transmission through a subwavelength aperture and the fundamental theorems of the surface plasma resonance (SPR) and localized surface plasmon (LSP) effect will be reviewed in this chapter. In addition, the numerical approximations, finite difference time domain (FDTD) solution, is briefly interpreted as well. The literature surveys are also including the morphing of the apertures and the surface corrugations at the end of this chapter.

2.1 Bethe's Theory

According to Bethe's theory [1], the transmission of a subwavelength hole in a very large, thin and perfectly conducting film, indicates the transmission, normalized to the area of the hole, scales as $(d/\lambda)^4$, where d is the hole diameter and λ is the wavelength, as shown in Fig 2.1-1. The result leads to extremely weak transmissions when $d>>\lambda$. Since the work of Bethe, the subwavelength apertures have been further analyzed theoretically. In fact, the practical phenomenon of real metal is a complex situation.

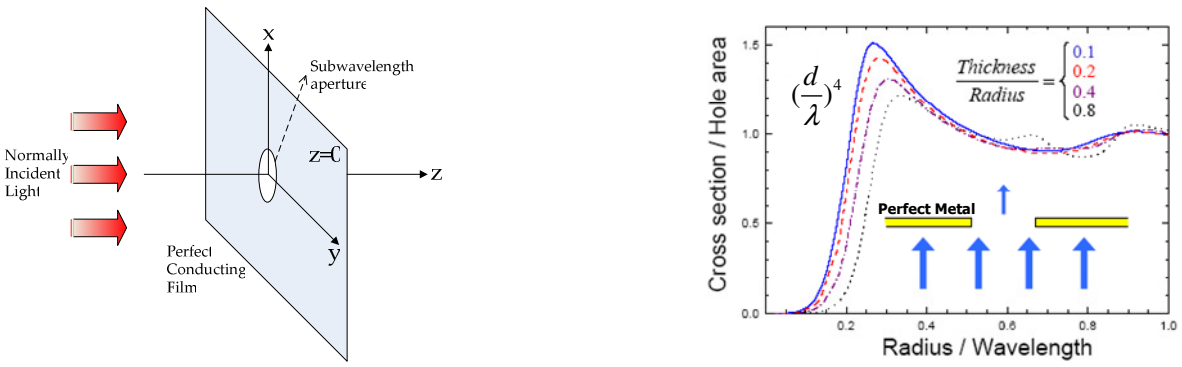

Fig. 2.1-1 Model of Bethe's theory and transmission cross section of a cylindrical hole drilled in a perfect-metal film as a function of the hole radius for different ratios of the slab thickness to the radius (see labels). The light is coming perpendicular to the film

2.2 Surface Plasmon Resonance

Since T.W Ebbesen *et al.* observed the extraordinary high transmission on 2-D periodic nanohole array [2-11]. Surface plasmon resonance (SPR) effect has drawn more attention to enhance the light transmission through the metallic subwavelength aperture. We will introduce surface plasmon resonance effect by the fundamental electromagnetism theory in this section [12].

To suppose an infinite large metal layer, as shown in Fig. 2.2-1

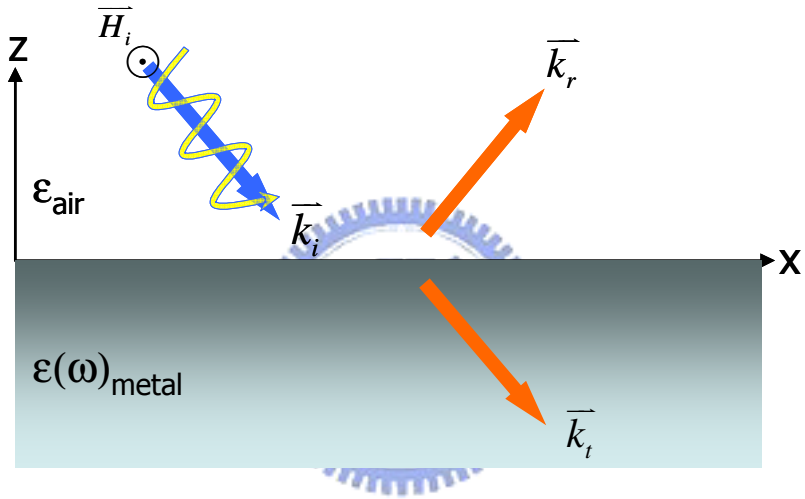

Fig. 2.2-1 Structures of surface plasmon excitation with TM-polarization incidence from air to metal. The metal was set in z < 0.

If the EM wave is incidence from dielectric media (z>0) to metal (z<0) and the polarization is TM (H_z=0), the electric field and magnetic field in dielectric media (z>0) could be written as [13]:

$$\vec{H}_1 = \begin{pmatrix} 0 \\ H_{1y} \\ 0 \end{pmatrix} e^{ik_{1z}z} e^{i(k_x x - \omega t)} \tag{2.1}$$

$$\vec{E}_1 = \begin{pmatrix} E_{1x} \\ 0 \\ E_{1z} \end{pmatrix} e^{ik_{1z}z} e^{i(k_x x - \omega t)} \tag{2.2}$$

Furthermore, in metal zone (z<0),

$$\overrightarrow{H}_2 = \begin{pmatrix} 0 \\ H_{2y} \\ 0 \end{pmatrix} e^{-ik_{2z}z} e^{i(k_x x - \omega t)} \tag{2.3}$$

$$\overrightarrow{E}_2 = \begin{pmatrix} E_{2x} \\ 0 \\ E_{2z} \end{pmatrix} e^{-ik_{2z}z} e^{i(k_x x - \omega t)} \tag{2.4}$$

Here we use parallel component of the wave vector k are equal in different media ($k_{1x}=k_{2x}$) directly.

According to Maxwell equations:

$$\nabla \bullet \overrightarrow{D} = \rho_f \tag{2.5}$$

$$\nabla \times \overrightarrow{E} = -\frac{\partial \overrightarrow{B}}{\partial t} \tag{2.6}$$

$$\nabla \bullet \overrightarrow{B} = 0 \tag{2.7}$$

$$\nabla \times \overrightarrow{H} = \frac{\partial \overrightarrow{D}}{\partial t} + J_f \tag{2.8}$$

$$\overrightarrow{D} = \varepsilon \overrightarrow{E} \tag{2.9}$$

$$\overrightarrow{B} = \mu \overrightarrow{H} \tag{2.10}$$

And the boundary condition

$$E_{1x} = E_{2x} \tag{2.11}$$

$$H_{1x} = H_{2x} \tag{2.12}$$

Where D is electric flux density, ρ_f is free electric charge density, E is electric field, B is magnetic flux density, H is magnetic field, J_f is free current density, ε is permittivity and μ is permeability. Since the system is source free, and the ε of the media we consider are only dependent on frequency (ε=ε(ω)), the dispersion relation about surface plasmon wave could be obtained.

$$\frac{k_{1z}}{\varepsilon_{air}} + \frac{k_{2z}}{\varepsilon(\omega)_{metal}} = 0 \tag{2.13}$$

In order to excite surface plasmon wave, $\varepsilon_{air}*\varepsilon_{metal}(\omega) < 0$ is the first condition, which is easily satisfied due to that the dielectric constant of metal can be negative in visible light range. On the other hand, the parallel component of wave vector k_x can be also written as

$$k_{xsp} = \frac{\omega}{c}\left[\frac{\varepsilon_{air}\varepsilon(\omega)_{metal}}{\varepsilon_{air}+\varepsilon(\omega)_{metal}}\right]^{1/2} \tag{2.14}$$

The absolute value $|k_{xsp}|$ is larger than the parallel component of wave vector of incidence. As shown in Fig. 2.2.2. The black line describes the general condition in the media without dispersion, and the red line shows the surface plasmon excitation dispersion condition. That means it is impossible to excite surface plasmon wave in general incidence from dielectric to metal. Some couple mechanism method to apply for higher parallel momentum k_x is needed. The primary two methods are going to be introduced briefly as following.

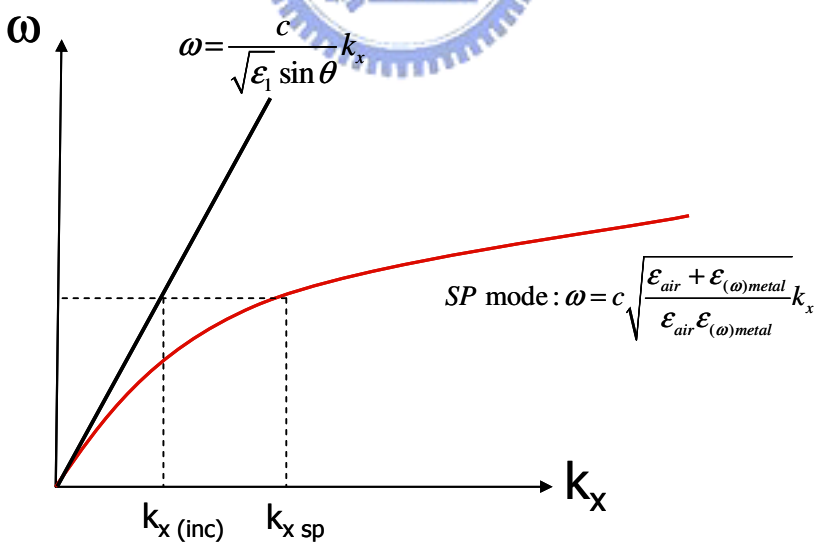

Fig. 2.2-2 Dispersion curve relation between light incidence in air and the surface plasmon mode.

2.2.1 Grating Coupler Method

We consider while light incident into a grating periodic structure, shown in Fig. 2.2-3.

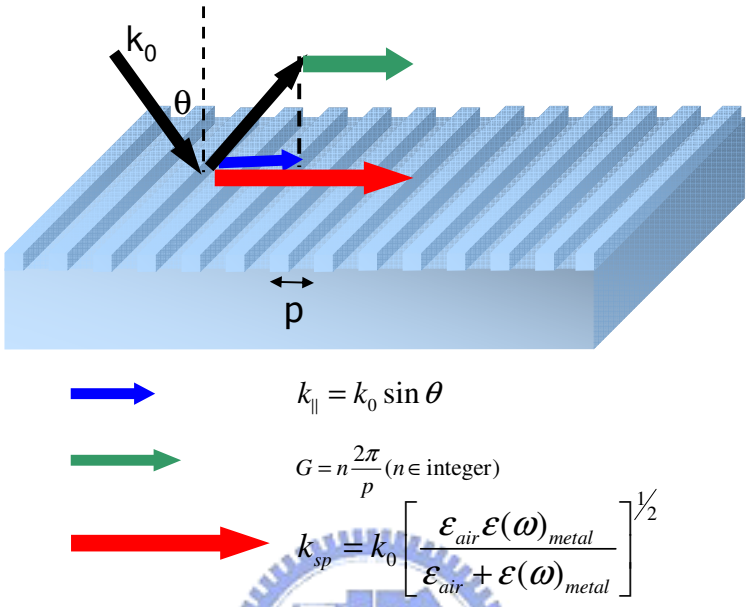

Fig. 2.2-3 Excitation mechanism of surface plasmon wave by grating coupler.

Due to the reciprocal lattice vector theory, the incident electric magnetic field would obtain (or lose) extra parallel momentum k_x. The mathematical formula is form of

$$k_{sp} = k_0 \left[\frac{\varepsilon_{air}\varepsilon(\omega)_{metal}}{\varepsilon_{air} + \varepsilon(\omega)_{metal}} \right]^{1/2} = k_0 \sin\theta + G \qquad (2.15)$$

According to the formula above, the parallel wave vector k_x would be enhanced by grating coupler. The dispersion curve would also be modified to match surface plasmon mode, shown in Fig. 2.2-4. The green-dash line shows the modified curve. We observe here that the surface structure period of metal would be a important role to excite surface plasmon resonance. On the other words, surface plasmon excitation might be easily driven by means of the surface structure of metal.

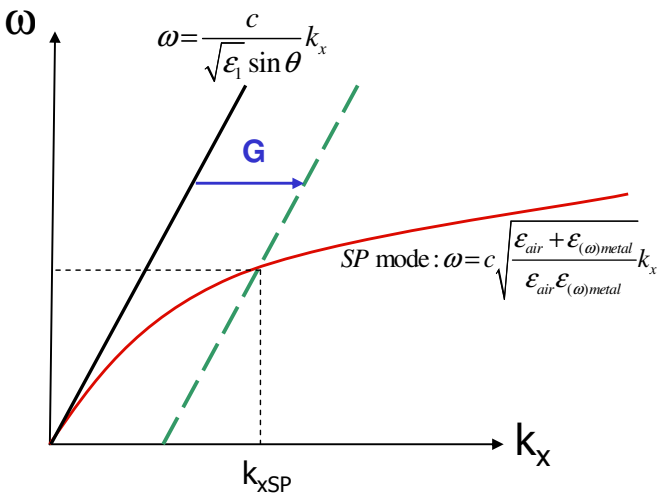

Fig. 2.2-4 Dispersion curve relation between light incidence in air (black-solid) and the surface plasmon mode (red), and the modified curve by grating coupler (green-dash).

2.2.2 Attenuated Total Internal Reflection (ATIR) Method

The other methods to induce surface plasmon wave are employing the higher dielectric constant (index of refraction) to enable the attenuated total internal reflection electric magnetic field. It can be taken into two configurations, Otto and Kretschmann named by the inventors, as shown in Fig. 2.2-5 While light incident into the a higher dielectric constant medium, the wave vector value k will be larger than in air; and further, the light with higher momentum k occurs the total internal reflection (TIR) at the interface between dielectric medium and metal film. The evanescent wave is going to be arisen at the interface on z-direction. It means that the z-component of wave vector should be imaginary, (i.e. $\mathbf{k}_z = ik_z$). Due to conservation of momentum, the x-component of wave vector k_x will become to be larger than of incidence. The mathematic derivation is given as:

$$k_{0(\varepsilon_2)}{}^2 = k_{x(\varepsilon_2)}{}^2 + k_{z(\varepsilon_2)}{}^2 \tag{2.16}$$

While $\mathbf{k}_z = ik_z$,

$$k_{0(\varepsilon_{air})}{}^2 = k_{x(\varepsilon_{air})}{}^2 + (ik_{z(\varepsilon_{air})})^2 \tag{2.17}$$

Obviously,

$$k_x{}'_{(\varepsilon_{air})} > k_{x(\varepsilon_{air})} = k_0 \sin\theta \tag{2.18}$$

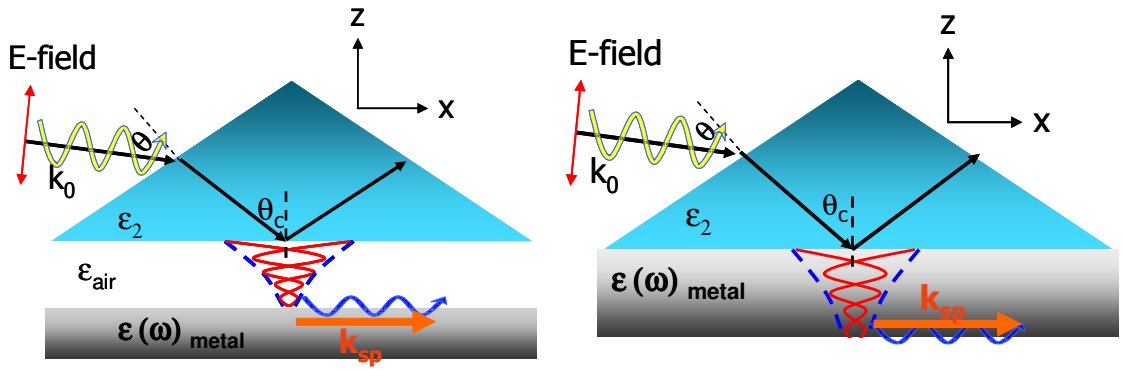

Fig. 2.2-5 Scheme of excitation mechanism of surface pasmon wave by attenuated total internal reflection (ATIR) method, Otto configuration (left) and Kretschmann configuration (right).

We might modify the dispersion curve to match the surface plasmon mode, as shown in Fig 2.2-6.

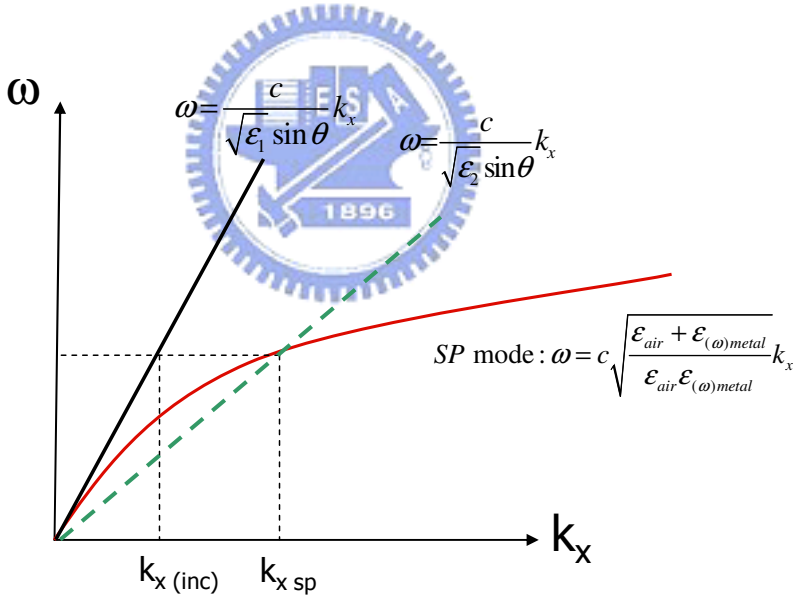

Fig. 2.2-6 Dispersion curve relation between light incidence in air (black-solid) and the surface plasmon mode (red), and the modified curve by ATIR coupler (green-dash).

2.3 A Subwavelength Aperture in Real Metal

In this section, we kept the eyes on the transmission behavior through a subwavelength metallic aperture. The studies include the characteristics of (a) polarization dependence, (b) spectrums analysis of the different subwavelength forms, and (c) the resonance with the thickness of film.

2.3.1 Polarization Dependence on the Geometric Shape of the Aperture

T.W. Ebbesen *et al.* [11]. have also analyzed the different subwavelength apertures, which are circular (symmetric) and rectangular (non-symmetric), to verify the existence of the localized surface plasmon (LSP). At the beginning, the measurement of the transmission of cylindrical holes with a given diameter (d=270 nm) for various hole depths h is shown in Figs. 2.3-1. The transmission for λ>600 nm is sensitive to the hole depth when λ>2d, no propagation mode could be sustained at the situation.

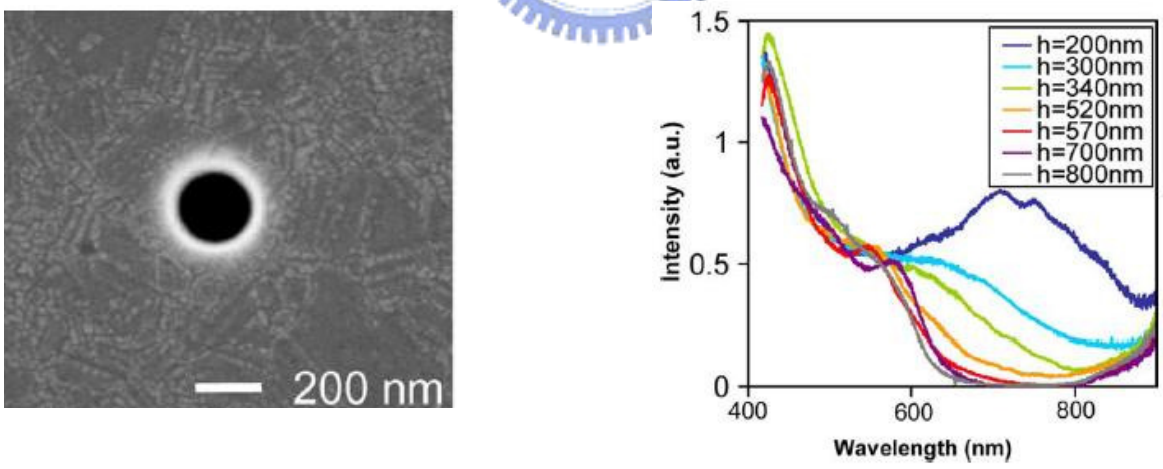

Fig. 2.3-1 (a) The SEM micrograph image of an isolated subwavelength aperture in a suspended Ag film. (b) Transmission spectra at normal incidence for cylindrical holes of diameter d=270 nm, for a range of hole depths h. Each curve is an average of the spectra of several isolated holes of the same dimensions.

Furthermore, the LSP can be clarified by examining rectangular subwavelength holes (Fig. 2.3-2) as well. The result exhibits the transmission spectrum of a rectangular aperture in a 700-nm thick silver (Ag) film for various incident linear polarizations. Two distinct peaks can be observed by simply changing the angle θ between the electric-field and the longitudinal direction. As θ varies from 0° to 90°, one switches from a mode at around 450 nm to another one at 700 nm. The intensity of the two peaks as a function of incident orientation θ obey the classical Malus law for polarization, which means that the LSP modes are launched by the components of the electric field orthogonal to the straight edge.

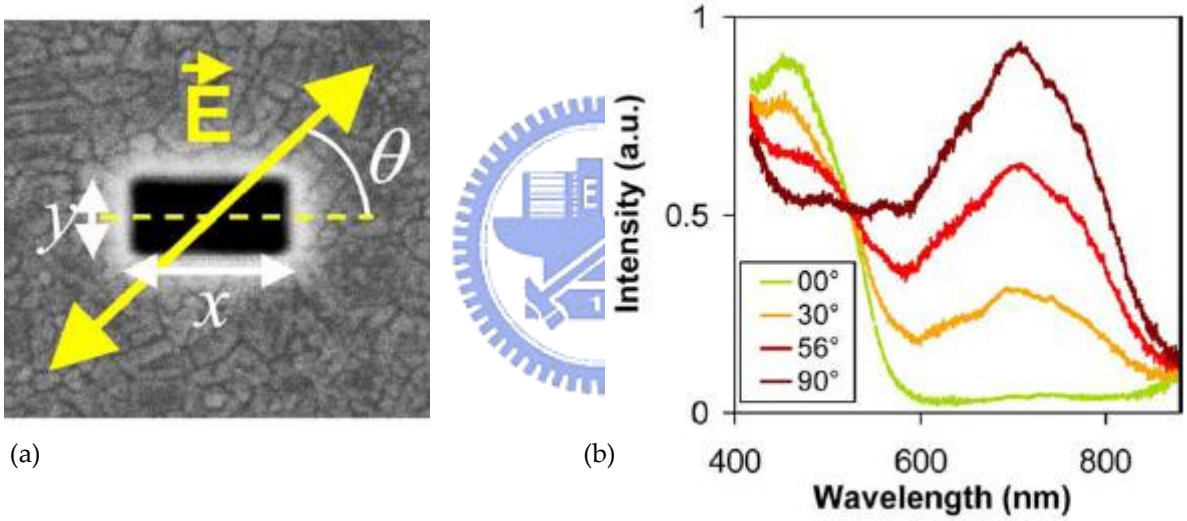

Fig 2.3-2 (a) SEM micrograph image of a rectangular aperture in a suspended Ag film. Also shown are the notations adopted in the text: θ is the angle between the electric field and the longitudinal direction, x(y) is the longitudinal (transverse) dimension of the rectangle. (b) Transmission spectra of an isolated rectangular aperture for various linear polarizations (h=700 nm, x=310 nm, y=210 nm).

The existence of a single peak in the spectra of cylindrical hole and the presence of two resonances for a rectangular aperture indicates the peak resonance wavelength is high dependence on the geometric structure of the aperture and the polarization of incidence.

2.3.2 Phenomena of Light Transmission through the 2-D Slit

The pioneer experimental researches from Ebbesen's group have been studied in previous introduction. At the same time, M. Mansuripur *et al.* do fruitful contributions on the theoretical discussions [14-16]. We are going to briefly summarize his conclusions. The details can be referred to [17].

The simulation conditions must be declared first such as a Gaussian beam of light incidence, having full-width at half-maximum intensity FWHM = 1.5 μm at the waist (located at z = 1200 nm) propagate along the negative z-direction. The vacuum wavelength of the light, λ_0 = 1.0 μm, is in the near-infrared range. A silver film (ε = 0.23 + 6.99 i at λ_0 = 1.0 μm) of thickness t centered at z = 0 has a slit aperture of width W. Since illumination is uniform in the x-direction and the setup is independent of x, Maxwell's equations are decoupled into $E_{\parallel}$ and $E_{\perp}$ modes, as indicated in Fig. 2.3-4 The $E_{\parallel}$ mode consists of Ex , Hy and Hz field components (Ex is along the length of the slit). The $E_{\perp}$ mode consists of Hx , Ey and Ez, with Ey being along the width of the slit.

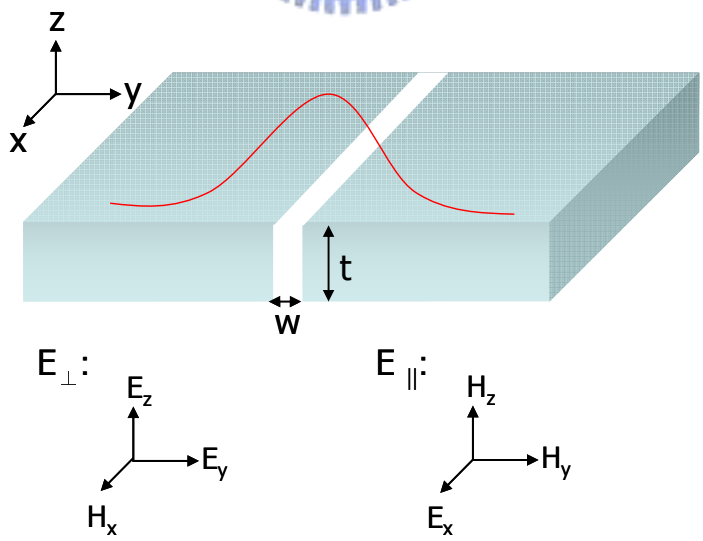

Fig. 2.3-4 A slit aperture of width W in a metallic film of thickness t. The material of the film (silver) has refractive index n + iκ = 0.23 + 6.99i and $\varepsilon = (n + i\kappa)^2 = -48.8 + 3.16i$ at λ_0 = 1.0 μm. The incident beam is uniform along x, and has a broad Gaussian profile along the y-axis; its linear polarization state, denoted by $E_{\parallel}$ or $E_{\perp}$, indicates the incident E-field direction relative to the slit's long axis. The relevant E- and H-field components for the two polarization states are shown below the slit.

While the width of slit is smaller than a half of wavelength of incidence ($W < 1/2\ \lambda_0$), the slit is also called "subwavelength" slit. According to the waveguide theory, the fundamental mode could not be sustained. Meanwhile, electric magnetic wave would not propagate under this condition. Anomalously, when the specific polarization of incidence was given, the stronger localized surface plasmon (LSP) will be a crucial role to make the light pass through the subwavelength slit is available in near-field range. The discussions aim at two orthogonal polarization of incidence was given as following.

(a) $E_{//}$ excitation:

The computational results with light transmission through subwavelength 2-dimensional slit ($W = 0.4\ \lambda_0$) under $E_{//}$ illumination were shown in Fig. 2.3-5. The E-field drops into the aperture, accompanying a rapidly decaying magnitude in the propagation direction −z. Since the E-field has no component perpendicular to the various metallic surfaces, no surface charges appear in this condition. The H-field lines bend into the aperture, then turn around and return to the incidence space. The surface currents that support the H-field in the vicinity of the various surfaces are everywhere in the x-direction.

Thus, the weak field below the aperture indicates that almost no light passes through. Another similar simulation for $E_{//}$ illumination also reveals the existence of a cutoff at $W < 1/2\ \lambda_0$ for guided waves through the slit. When $W < 1/2\ \lambda_0$, very little light could get through the slit, and the incident optical energy, aside from a small fraction that was absorbed within the metal's skin depth, was reflected back toward the source. The results almost match the waveguide theory as we may expect.

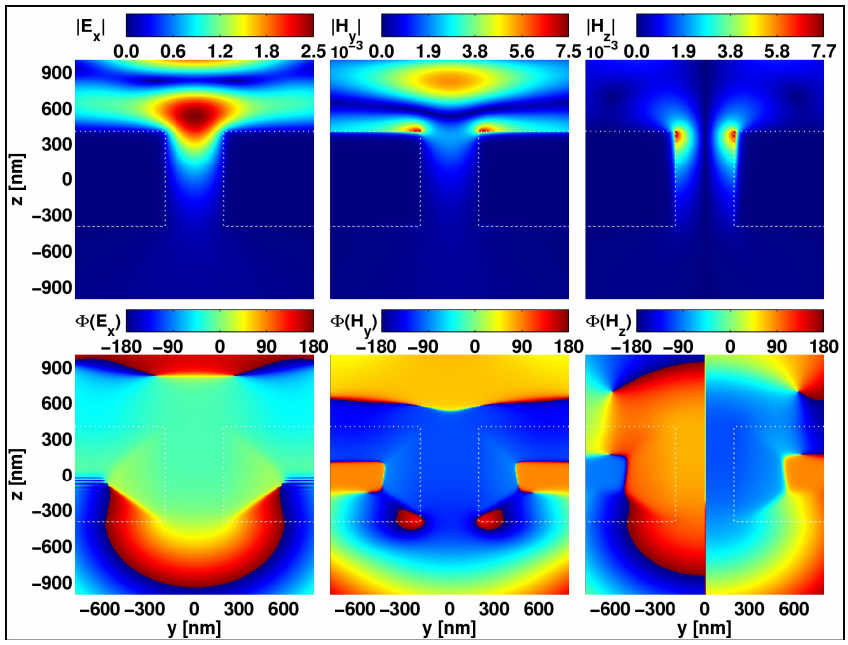

Fig. 2.3-5 Computed plots of Ex , Hy and Hz for the case of E∥ illumination: (top) magnitude, (bottom) phase. Film thickness t = 800nm; slit-width W = 400nm < 1/2 λ_0.

(b) E⊥ excitation:

In contrast, when the polarization of incidence is E⊥, the simulation results will be totally different. As shown in Fig. 2.3-6. The slit supports a guided mode, whose partial reflection at the bottom of the aperture is responsible for the observed interference fringes in Ey and Hx through the depth of the slit. The E-field plots show the accumulation of electrical charges at various locations on the metallic surfaces; in particular, Ey and Ez at the four corners of the slit show the presence of a strong dipole at the top, and a slightly weaker dipole at the bottom of the slit; the top and bottom dipoles have nearly the same phase. Additionally, Ey shows a periodically varying surface charge density through the slit's depth. The surface currents that support the magnetic field Hx near the metallic surfaces travel in the ± y-direction on the top surface and in the ± z-direction along the slit walls. These currents not only sustain the adjacent H-fields, but also (through their non-zero divergence) produce the surface charges.

According the discussion above, the light transmission is large than before (for $E_{//}$ excitation). It exhibits that the absence of a cutoff for $E_{\perp}$ illumination, even for an aperture as narrow as W =100 nm(<< 1/2 λ_0). The transmission could not be precessly explained by the waveguide theory since the subwavelength slit (W = 400 nm < 1/2 λ_0 is below cutoff) is applied.

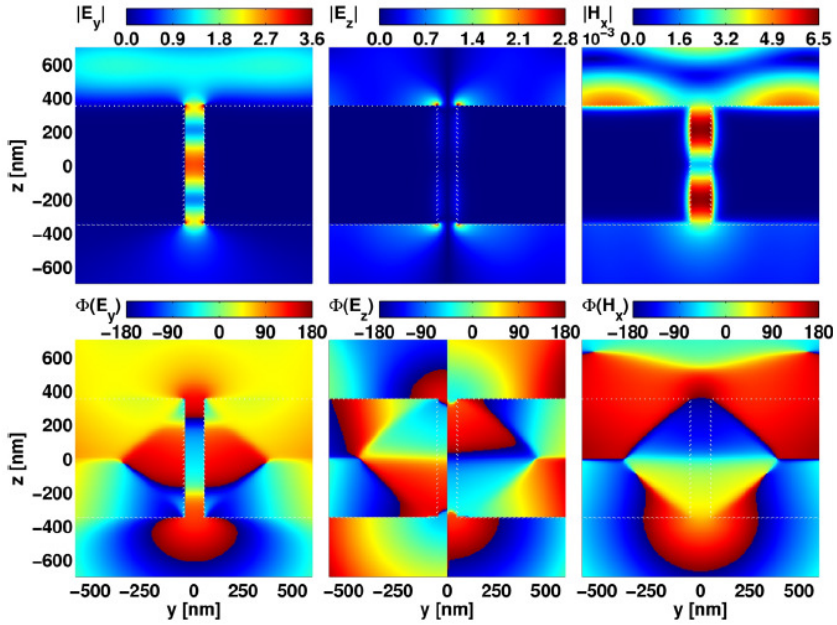

Fig. 2.3-6 Computed plots of Ey, Ez, Hx for $E_{\perp}$ illumination: (top) magnitude, (bottom) phase. t = 700 nm; W = $\lambda o/10$ = 100nm.

Furthermore, the dependence of $E_{//}$ and $E_{\perp}$ transmission on film thickness has also been discussed. The computation result is shown in Fig. 2.3-7. In Fig. 2.3-7(a), the component S_z of the Poynting vector at the output aperture for films of differing thickness t is given; the slit width is fixed at W = 100 nm and illumination is $E_{\perp}$. From the figure the transmission efficiency η is seen to be almost 200% when t = 300 nm and 700 nm, but only 70% when t = 100 nm, 500 nm, and 900 nm.

Fig. 2.3-7(b) shows plots of S_z at the output aperture under $E_{//}$ illumination for several values of the film thickness, when W = 400nm < 1/2 λ_0 (i.e., below cutoff). The graphs indicate S_z decays rapidly although there is some transmission for very thin

films with the increasing of film thickness until transmission essentially drops to zero beyond t ~ λ_0. Increasing the slit-width above W = 1/2 λ_0, however, removes all obstacles to transmission.

As shown in Fig. 2.3-7(c), when W = 600nm, transmission efficiency η in the middle of the slit is ~ 200%, and the dependence of S_z on film thickness is rather insignificant.

Fig. 2.3-7(d) is a summary of the results for both $E_{//}$ and $E_{\perp}$ illumination; here the integrated S_z immediately after the apertures studied in (a) - (c) is displayed as function of film thickness t. For $E_{\perp}$, the transmitted optical energy is seen to vary periodically with thickness (period ~ 400 nm); the curve's envelope drops gradually because of the absorption in the slit walls. For $E_{//}$, the throughput of a narrow aperture (W = 400 nm) drops exponentially with film thickness, but remains fairly constant for an aperture above the cutoff (W = 600nm).

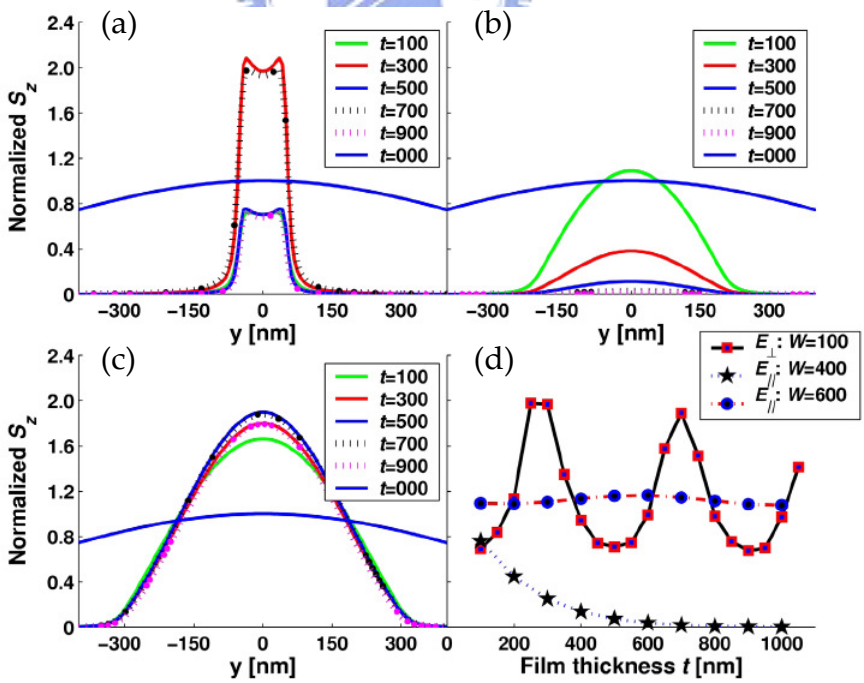

Fig. 2.3-7 Computed plots of the energy flux density S_z at the output aperture (z = −½ t) for different film thicknesses ranging from t = 100 nm to 900 nm. The broad blue line in (a)−(c) represents the incident beam's S_z at z = 0 (in free-space). (a) $E_{\perp}$ illumination, W = 100nm; (b) $E_{//}$ illumination, W = 400nm; (c) $E_{//}$ illumination, W = 600nm; (d) total transmitted S_z versus t for the slits depicted in (a)−(c).

2.4 Aperture Reforming

Although Bethe's theory predicted the power throughput of a subwavelength aperture is proportional to the quartic of its size, this statement may fail if those supported premises are invalid. One of the used approaches is to reform the aperture shape so that the assumption of symmetric and circular apertures is subverted [18-21]. This section will show several novel nano-apertures in sort of the literature time.

2.4.1 Triangular Aperture

A triangular aperture is regarded as an equilateral triangular pyramid of which the bottom portion is truncated [19],proposed by K. Tanaka *et al*. as shown in Fig. 2.4-1.

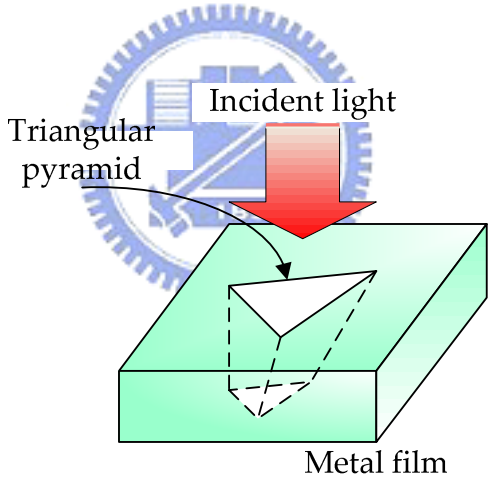

Fig. 2.4-1 Model of a near-field optical head with a triangular aperture

As shown in Fig. 2.4-2 the energy distribution is highly strengthened at the side perpendicular to the incident polarization; thereby, the double-peak effect can be eliminated. The transmitted power of a triangular aperture is several times higher than that of a conventional circular aperture; however, this is insufficient for the practical used, particularly for a dynamic data retriving

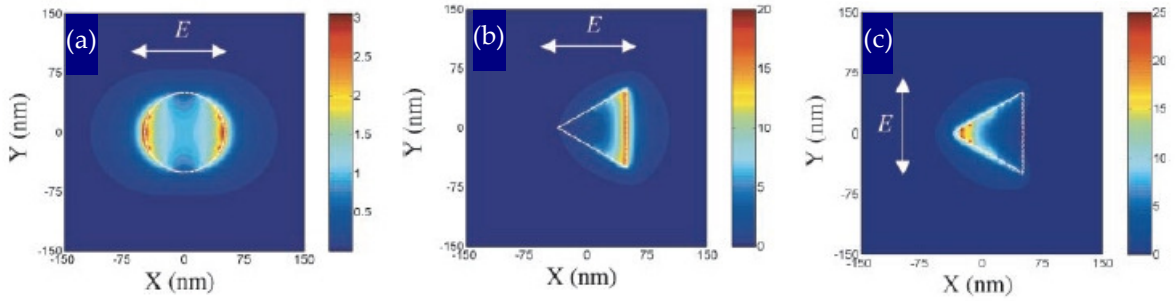

Fig. 2.4-2 Energy distribution of (a) a circular aperture with X-polarized incident light, and a triangular aperture with (b) X-polarized and (c) Y-polarized incident light. The aperture shape is outlined in each figure. Note the different color scaling in each figure.

2.4.2 I-shaped (or H-shaped) Aperture

A more complicated aperture is I-shaped (or H-shaped) aperture as plotted Fig. 2.4-3. All the dimensions of the I-aperture and the metal film are expressed as the multiples of the incident wavelength λ [20]

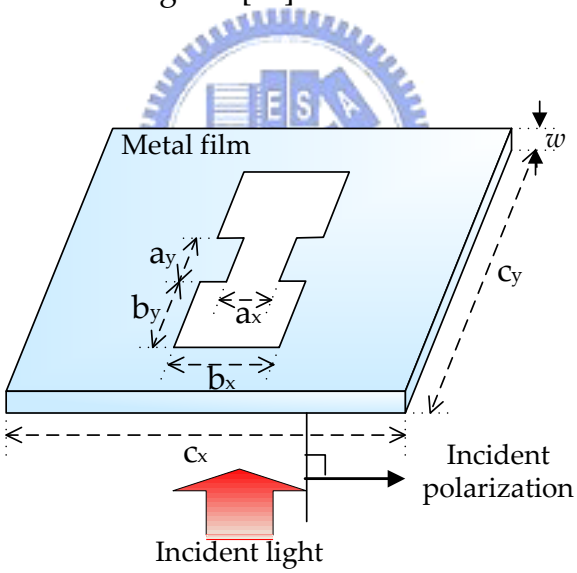

Fig. 2.4-3 Parameters of an I-shaped aperture

The comparison between a square aperture and an I-aperture, of which the gap area, ax*ay, is identical to the square aperture area, is displayed in Fig. 2.4-4, clearly showing the gap determines the transmitted power and the spot size principally. According to the simulations, the spot size is evidently reduced but the transmitted power is enhanced with a limited extent ~6X, which can compete with the triangular

apertures. Moreover, the I-aperture requires more complicated fabrication and will restrict its feasibility accordingly.

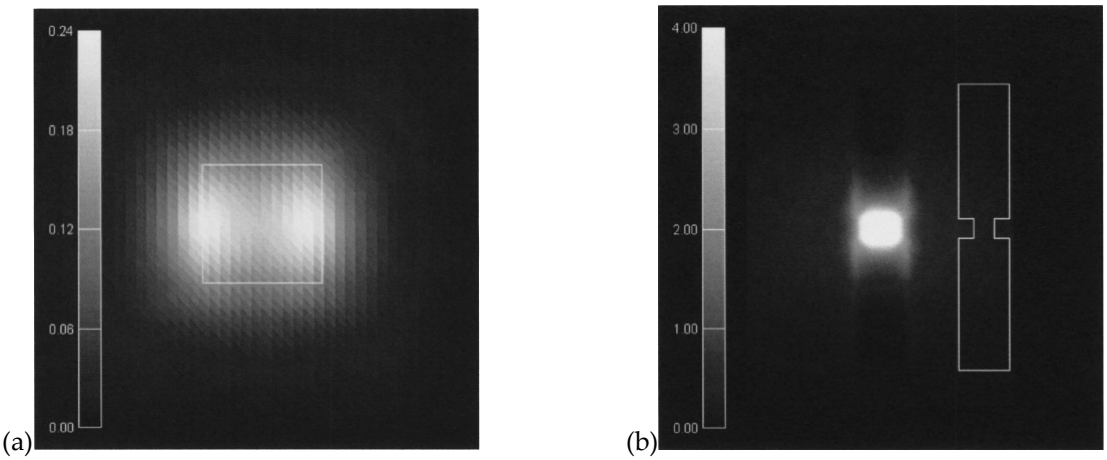

Fig. 2.4-4 Electric energy distribution of (a) a square aperture of 0.064λ*0.064λ and (b) an I-aperture with gap area of 0.064λ*0.064λ, the film thickness of 0.224λ and the dielectric constant of the film material of -7.38-i7.18

2.4.3 C-shaped Aperture

The C-shaped aperture [21] is another novel design, which is modeled in a perfect conducting film with X-polarized incident light, as shown in Fig. 2.4-5.

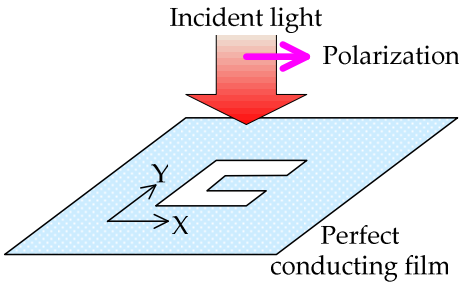

Fig. 2.4-5 Optical model of the C-shaped aperture

Compared with a 100*100 nm^2 square aperture, the power throughput of the C-aperture at the distance of 48 nm from the aperture is 1000X stronger with a comparable near-field spot size, as displayed in Fig. 2.4-6. However, the incident light wavelength in this model is 1 μm whereas most optical storage or detect systems are operated in the visible light regime where the natures of metals are

significantly depends on the wavelength of incidence. As a result, the behavior of such a C-aperture in visible light range is a pending problem to investigate.

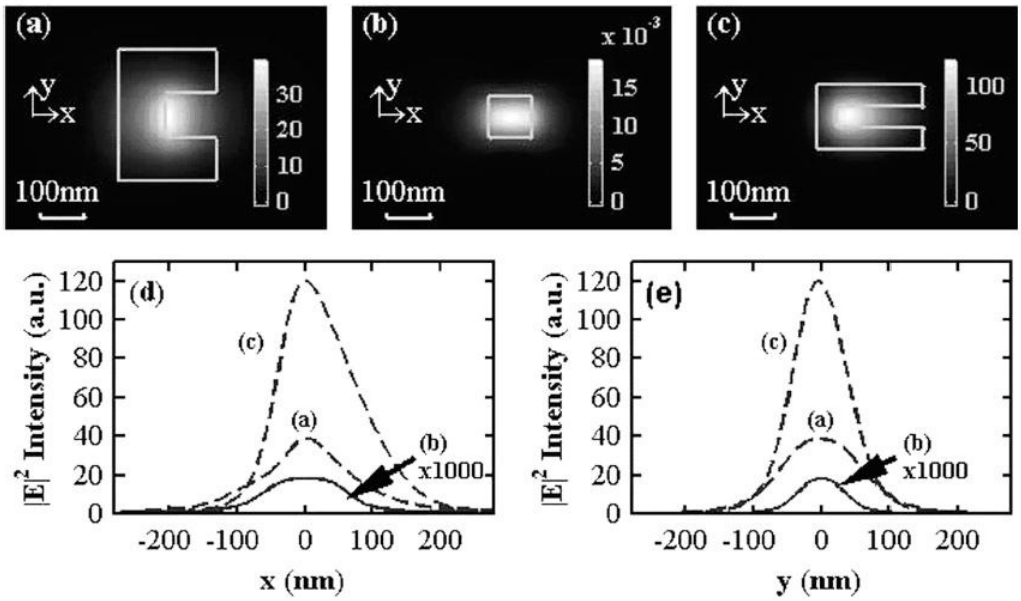

Fig. 2.4-6 |E|² distribution at 48 nm from the three apertures. (a) C, (b) square, (c) improved C with smaller spot size and higher intensity. Aperture geometries are outlined. (d), (e) j*E*j2 cross sections for the three apertures; the intensity is multiplied by 1000 for the square aperture.

2.5 Surface Corrugation

In 1998, Ebbesen *et al.* found that arrays of subwavelength apertures performed highly unusual zero-order transmission spectra [5], which is a sever challenge to Bethe's theory. In Ebbesen's study, a 200-nm-thick silver film was deposited on a quartz substrate and subsequently milled by focused-ion-beam (FIB) to fabricate aperture arrays. The distinct features of the transmission spectrum are the two phenomenal peaks took place at two wavelengths; one is a little larger than the pitches and the other one corresponds to 10X aperture diameters. Such two peaks show an evident overthrow of Bethe's formula that stated transmission is proportional to the quartic of the aperture size.

A further configuration attracting more attention is an aperture with surface corrugations [7], which allowed extraordinary transmission similar to aperture arrays as well. The structure was a free-standing Ni film of 300 nm thickness

sandwiched in Ag layers, subsequently perforated an aperture and patterned grooves as the surface corrugation by utilizing FIB, as shown in Fig. 2.5-1.

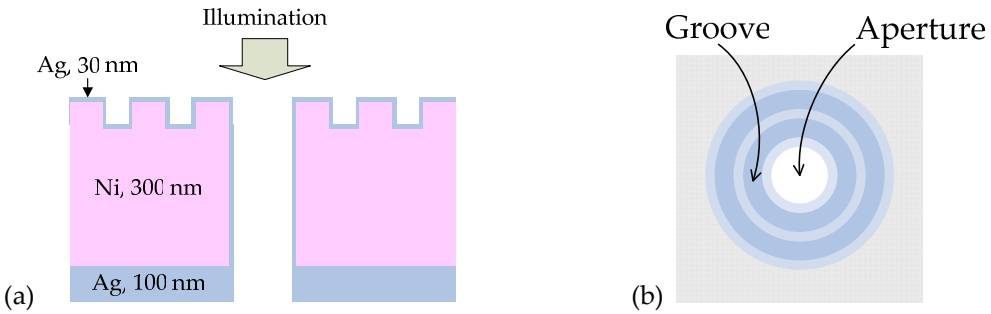

Fig. 2.5-1 The (a) side view and (b) top view of a single aperture surrounded by surface corrugations

Transmission through this configuration reaches the maximum at the wavelength approximate to the pitch of the corrugations; in addition, the transmission efficiency (transmission normalized to the aperture area) at the peak can be up to 2.6, as shown in Fig. 2.5-2, indicating even those photons not impinging on the aperture are also captured and emitted through the aperture. This phenomenon results from the resonance and coupling effect between the antisymmetric SPP modes and incident photons, which conduces the aperture acting as a novel probe of SPPs.

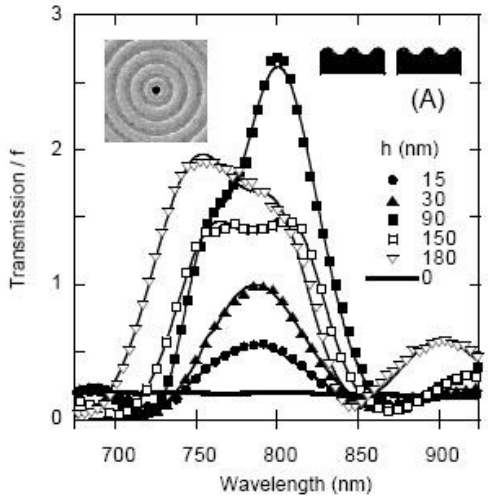

Fig. 2.5-2 Transmission spectra of a single aperture of diameter 440 nm surrounded by surface corrugation of pitch 750 nm with various corrugation depth h, the vertical axis is the ratio of transmission to aperture area.

Going a step further, if the exit side is also corrugated, the emitted light is highly directional, indicating the exit corrugation plays a role as a focusing grating. A plot of the transmission intensity as a function of angle at the resonant wavelength of 660 nm displayed in Fig. 2.5-3 shows the divergent angle (defined by Full-Width Half-Maximum) is only 5°. Such a discovery is exhilarating because it implies the working distance between the probe and the recording material can be enlarged.

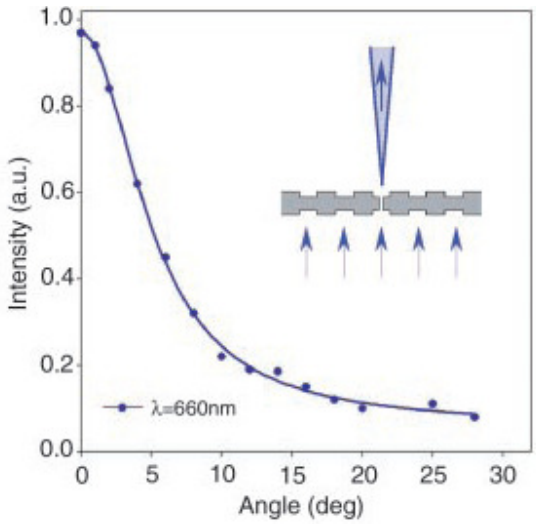

Fig. 2.5-3 Angular dependence of the transmission at the resonant wavelength of a double-corrugated configuration.

According to the aforementioned theory in section 2.2, the SPP modes can be excited on the exit surface as well so that the exit corrugations may not only function as a focusing grating but also contribute to the transmission enhancement by drawing supports from the coupling effect between SPP modes on the opposite side. In addition, the mechanism of such double-corrugated configuration can be divided into three independent procedures: coupling in, tunneling and coupling out; therefore, the parameters of trenches on the different sides can be optimized individually and enhancements can then be significant.

2.6 Simulation Method and Drude model

2.6.1 Finite Difference Time Domain Method

Since the exact analytical solutions to the practical electro-magnetic problem are often formidably difficult, it is necessary to apply numerical approaches. Finite-difference time-domain (FDTD) method is one of the most powerful approaches owing to its rigorous calculation without any physical assumptions or premises. Its chief notion is to discretize Maxwell equations by using central difference operators to replace the differential operators in both time and space variables [22].

While **E** and **H** fields are represented by their discrete values on the spatial grid and are advanced in time steps of Δt, the components of the vector fields **E** and **H** are staggered so that every component of the **E** field is surrounded by the **H** field's four circulating components and vice versa, as shown in Fig. 2.2-1. The contour integrals of **E** (or **H**) along the cell's edges in Faraday's (or Ampere's) law circulate around the corresponding **H** (or **E**) field components at the cell face's center. Additionally, several commonly used material-dispersion models such as Debye, Drude, or Lorentz can be readily incorporated with the time-dependent formulation [23] via either a linear recursive relation [24] or auxiliary differential equation methods [25].

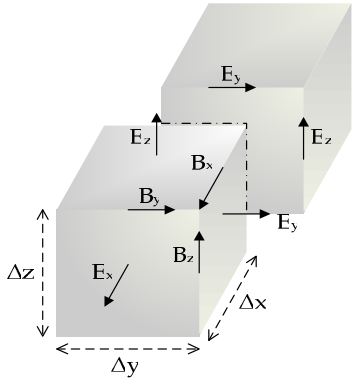

Fig. 2.6-1 Unit cell of FDTD mesh, components of **E** and **H** field are shifted by a half-pixel in x, y, z directions so that each **E** field component normal to the cell face is surrounded by the circulation of those **H** field components defined on the cell edges.

In 3D simulations, at least six field components must be stored and updated at each grid point, which leads to considerable memory consumption and CPU requirements. Fortunately, the time update of any field component involves only nearby fields located one or two cells away from the grid. This kind of locality in the physical space translates into computer memory access locality and allows for efficient implementation of FDTD algorithm on shared and distributed memory parallel platforms.

The boundary condition is a critical issue for FDTD method. In most of cases, low-reflection boundary conditions, such as Mur's absorbing boundary and the perfectly matched layer (PML) boundary condition [23], are popularly applied for those problems requiring open boundaries to simulate propagation into infinity. Furthermore, combining the total-field or scattered-field techniques [23] for the source-field distribution will allow accurate evaluation of the incident, reflected, and transmitted waves throughout the computational domain.

Although the numerical discretization in FDTD method does not introduce additional dissipation into the physical problem, it contributes to the numerical dispersion error in mathematics. In the commonly used implementation of FDTD, this error is proportional to the cell size h as a second order error function, $O(h^2)$. Practically, in order to keep the numerical dispersion errors under control, a grid with about 30 points per wavelength is anyhow desired.

2.6.2 Drude model

Drude model [26] assumes that there has no any other interaction between free charge (electronics) and nucleus. While applying the external electric field, the free charge's behavior follows Newton's law of motion. In addition, all the collisions inside the lattice are elastic. The complex relative permittivity ε_r in conductors can be written as:

$$\varepsilon_r(\omega) = 1 + \frac{i\sigma(\omega)}{\varepsilon_0 \omega} = 1 - \frac{\omega_p{}^2}{\omega^2 + i\omega\gamma_D}$$

Where σ is conductivity, $\omega_p = (\frac{Ne^2}{m\varepsilon_0})^{\frac{1}{2}}$ is plasma resonance frequency of metal, N is the electron density, m is the effective mass of the conduction electrons. In the range of $0 < \omega < \omega_P$, the dielectric constant is negative and no modes are allowed in the bulk of the metal. It accounts for the metals are extremely opaque at optical frequencies.

2.7 Summary

This chapter surveys the fundamental principles of surface plasmon resonance, and stimulates `the thought of a special shaped aperture surrounded by the surface corrugations to come into being. Among those special shaped apertures, Ridge-based aperture merits the favors because of the several orders of magnitude field enhancement. Consequently, optimizing Ridge-based aperture dimension to achieve satisfactory optical performance is the first step and the surface corrugations will be introduced sequentially for further field enhancement and spot size reduction.

Chapter 3 Aperture Morphing – Simulations

To demonstrate the optical delivery of the subwavelength aperture, at first simulation is carried out as a guide to the fabrication. This chapter focuses on the discussion and optimization of the subwavelength aperture, including the transmission mechanism of the aperture and spot performance at exit plane.

3.1 Optical Model

The simulation model is depicted in Fig. 3.1-1. A plane wave propagating toward +z. The two orthogonal polarized excitations were considered separately. Since the spot size for general incident light is much larger than the aperture area, the incident light can be considered as a plane wave normally into the aperture.

In addition, the dispersion relation of the silver film with n (refraction index) and κ (absorption index) [27] versus wavelength of incidence is shown in Fig. 3.1-2, which implies the skin depth of ~30 nm at wavelength of incidence λ=633 nm. We should note that the film thickness must be larger than it to prevent the light from leaking accordingly.

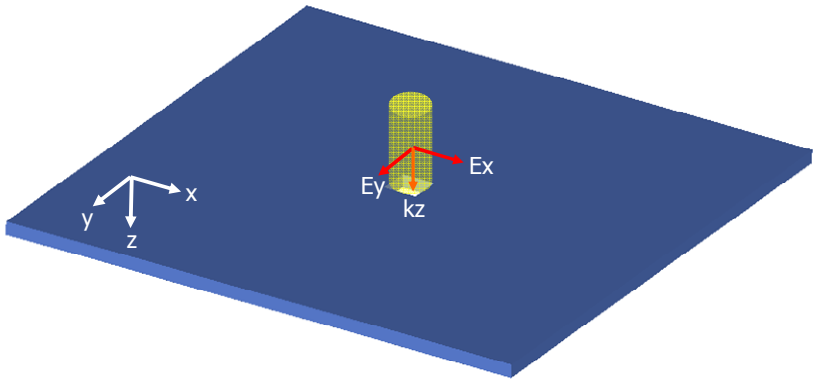

Fig. 3.1-1 Schematic diagram of the relation between the polarization of incidence and the subwavelength aperture.

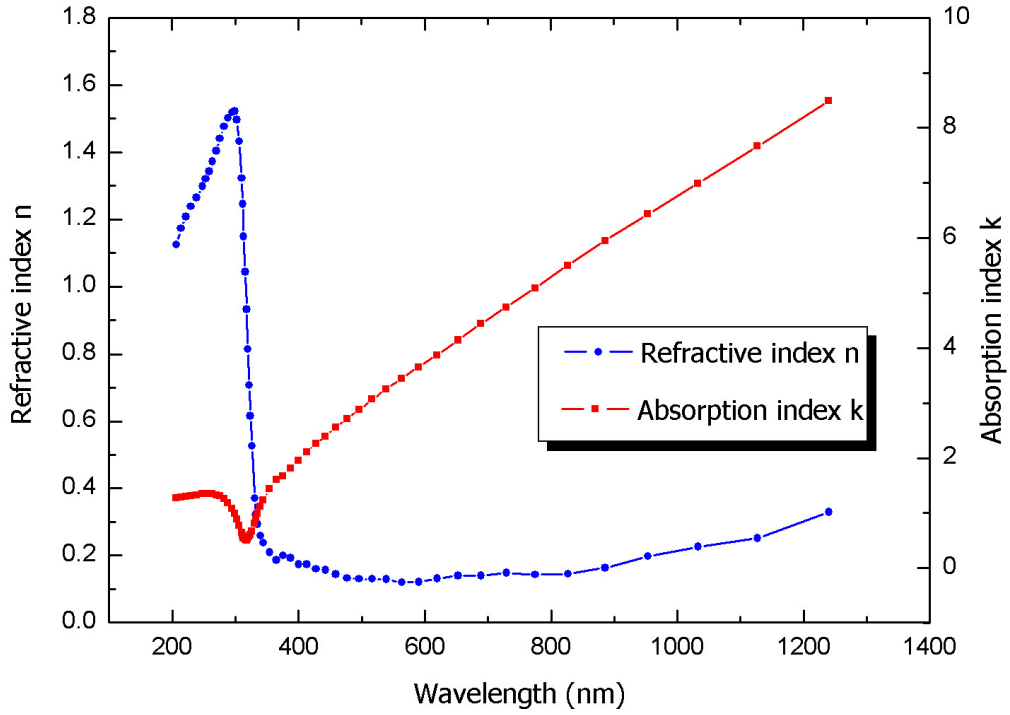

Fig. 3.1-2 The relation between n(refractive index), κ(absorption index) and wavelength of incidence.

Moreover, the curve above also exhibits the refractive index n is always ~0.14, and the absorption index κ is linear trend in visible range (400 nm ~ 800 nm). The evaluation factors applied in this thesis are going to be introduced as following.

(a) Power throughput (PT): Power throughput (PT) is dimensionless and defined as the ratio of the total transmitted power to the product of incident power density and the aperture area.

$$PT=\frac{\text{Total transmitted power}}{\text{Incident power density}\times\text{Aperture area}}$$

Its physical meaning is to quantify the photon capturing ability of the aperture. PT less than unity indicates the photons even impinging on the aperture cannot tunnel through the aperture whereas excess over unity signifies those incident

photons beyond the aperture area can still be captured, as schematically plotted in Fig. 3.1-3.

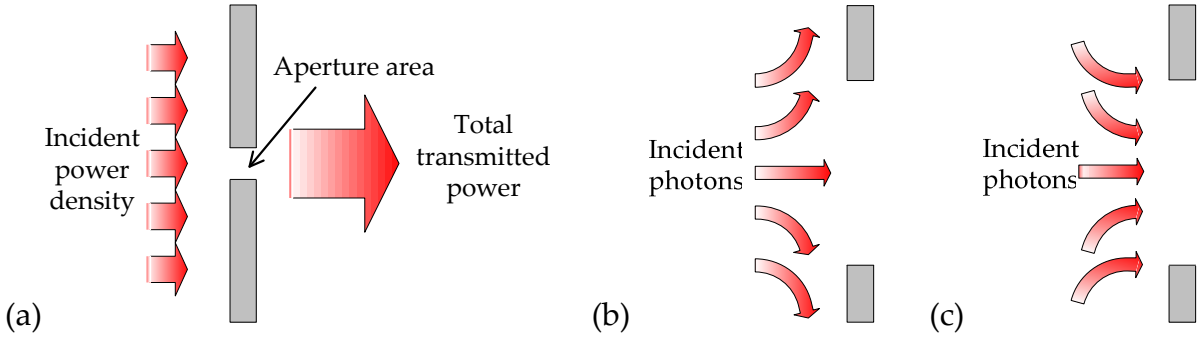

Fig. 3.1-3 Schemes of (a) power throughput, (b) photons incapable of tunneling and (c) photons captured by the aperture

(b) Power throughput density (PTD): Power throughput density is defined as the ratio of power throughput to the spot size.

$$\text{PTD} = \frac{\text{Power throughput}}{\text{Spot size } S_x \times \text{Spot size } S_y}$$

Spot size is the area that tunneled photons spread out and can be considered as the photon delivering ability of the aperture accordingly. From this perspective, PTD can be interpreted as

$$\text{PTD} = \frac{\text{Photon capturing ability}}{\text{Photon escaping ability}}$$

Therefore, PTD can appropriately evaluate the optical performance of an aperture thoroughly because it takes both incidence and emission into consideration simultaneously.

3.2 Simulations and Discussions

3.2.1 Square Aperture

A square or circular aperture is often applied in the subwavelength aperture research instinctively. It also serves as a reference for other shapes.

In the beginning, we made the spectrum analysis of square aperture (60 *60 nm^2). The square aperture transmission spectrum shown in Fig. 3.2-1 decreases quartically with the incident wavelength and the fitted polynomial reveals the tendency following Bethe's formula. The assumptions of Bethe's formula have been discussed in chapter 2. Although the simulation conditions here did not accord with the assumption exactly, the results show the formula still works under the similar environment.

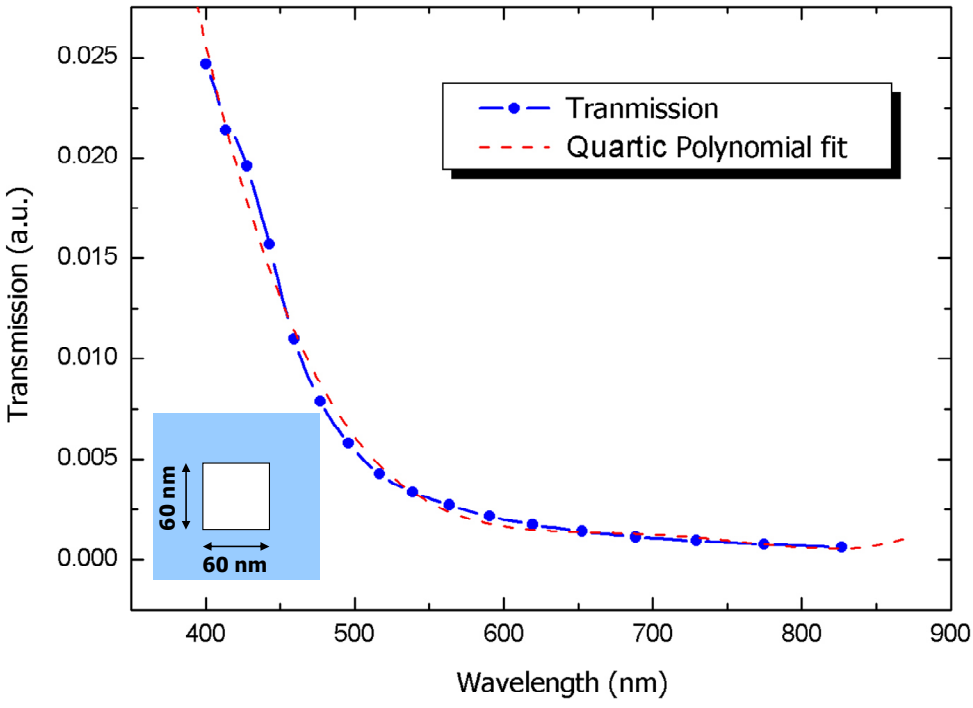

Fig. 3.2-1 Transmission spectrum of at normal incidence for square aperture (60 nm*60 nm), and thickness of film is 200 nm

Due to the X-polarized incident light, the spot size is elongated in X-direction depolarization effect, as shown in Fig. 3.2-2. The spot size is 141*122 (nm^2) defined by FWHM (Full Width at Half Maximum). Furthermore, the peak value of the energy density distribution is ~10^{-5}. It means the energy passed through the square aperture is very weak.

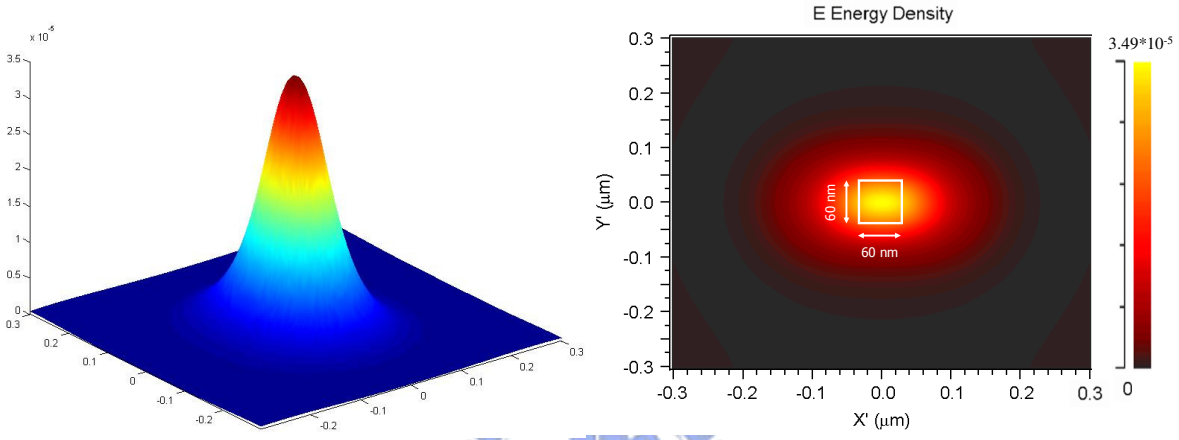

Fig. 3.2-2 E-field energy density distribution of square aperture (60 nm*60 nm) and the thickness is 200 nm for λ=633 nm, the observation plane is at 50 nm from exit plane.

Moreover, Fig. 3.2-3 plots the Poynting vector and field distribution at entrance plane (the direction of incidence is +z), which shows the energy flow clearly. The most part of energy is reflected backward to the source or absorbed by metallic surface. Even if the small fraction of energy propagates into the aperture, decays rapidly inside aperture. The fundamental mode does not come into exist in this case. It is coincident with the waveguide theory wave can not propagate under cut off condition d < 1/2 λ.

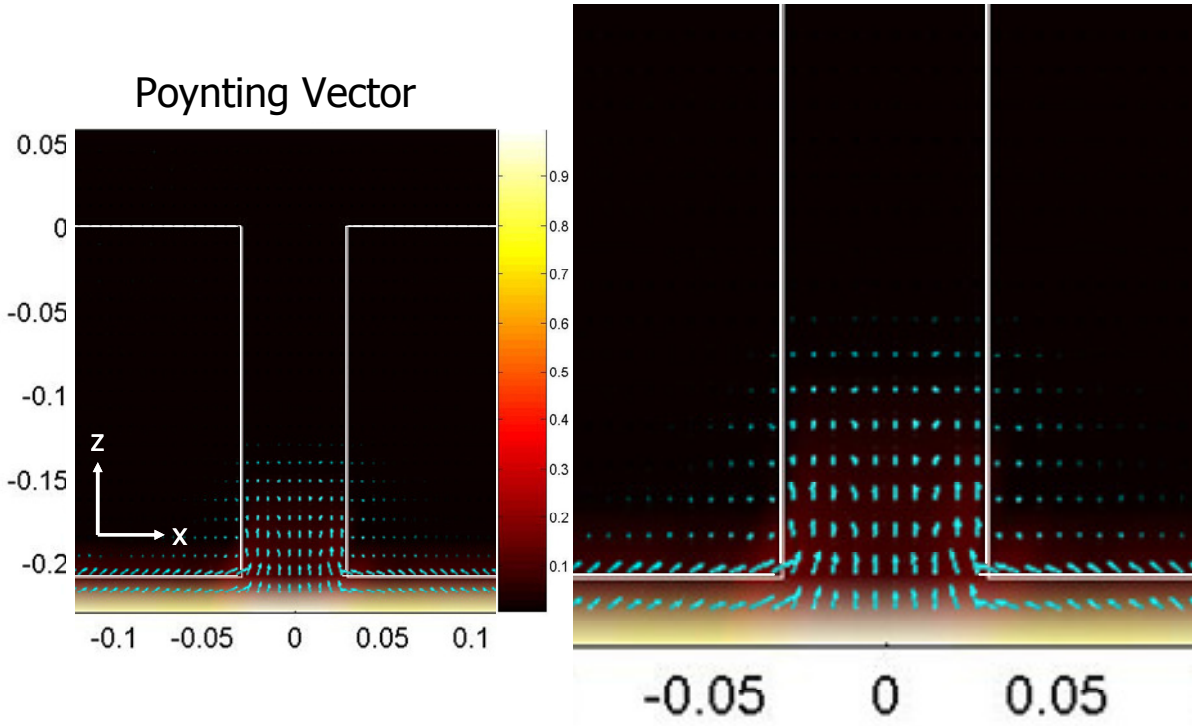

Fig. 3.2-3 Plot of Poynting vector on X-Z plane for square aperture (60*60 nm²) (left) and zoom in image (right)

We continue to consider the role of thickness in the above case discussed above. Fig. 3.2-4 exhibits the transmission versus the film thickness.

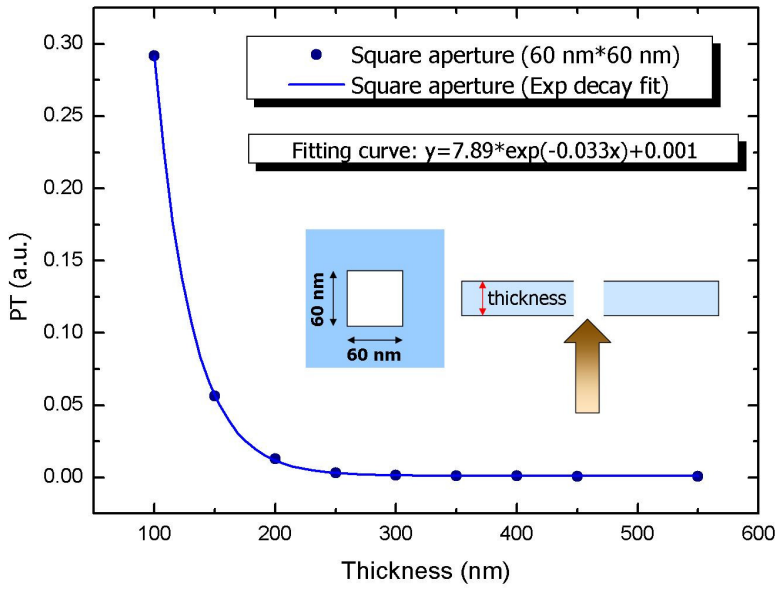

Fig. 3.2-4 Transmission versus film thickness for square aperture (60*60 nm²) and λ=633 nm.

It indicates the thickness of metal film (silver film for λ=633 nm) is a barrier for the transmission of square apertures. The transmission decreases exponentially with gradual increasing thickness. Transmission almost disappears when thickness approaches only to 300 nm, where the skin depth is ~30 nm.

Since the discussions of the power throughput and transmission for square aperture have been given above, the spot size produced by the aperture is also an important issue in the topic. We could pay more attention to the polarization effect on the spot size. The simulation results of spot size for various side width was shown in Fig 3.2-5. While the polarization of excitation is on X- direction, the spot size on the same direction is wider than the other (Y-) direction. The trend of the curve indicates the spot size is related to side width of aperture directly. In addition, the higher transmission could be obtained form the larger aperture, which also make the spot larger. The trade off between high transmission and smaller spot size is the main issue, especially on the apertures which is symmetric on both X- and Y-polarization directions.

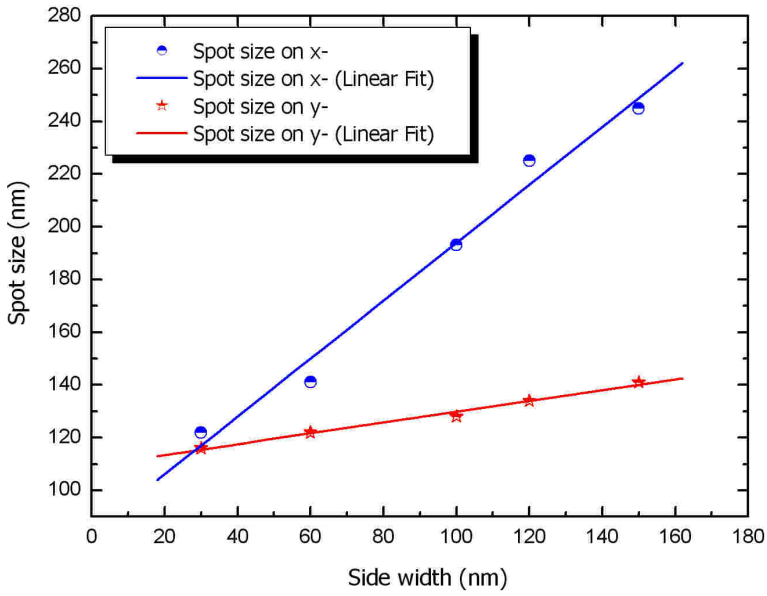

Fig. 3.2-5 Spot size at individual direction of various side width for square aperture.

Another phenomenon is the trend of X- and Y- directions are independent. The X- direction curve grows up rapider than Y- when side width of aperture increase. That provides that the X- polarized incidence make the same direction (X-) is more sensitive the Y- on field distribution.

Considering different refractive (n) and absorption (κ) indices with various wavelength. The computational results reveal the spot have overcome the diffraction limit, however, the transmission or power throughput (PT) is so weak that will be a problem in the system.

Table 3.2-1 shows the results about square aperture with different width. They might be a landmark for following discussions.

Table 3.2-1 Comparisons of square aperture with different side width, the wavelength of incidence is λ=633 nm.

Aperture (nm^2)	Transmission (a.u.)	PT (a.u.)	Spot Size (nm^2)	PTD (μm^{-2})
30*30	4.71×10^{-4}	9.82×10^{-3}	122x116	6.94×10^{-1}
60*60	1.28×10^{-3}	1.33×10^{-2}	144x122	7.59×10^{-1}
100*100	1.15×10^{-2}	7.21×10^{-2}	193x128	2.92
120*120	2.59×10^{-2}	1.35×10^{-2}	225x134	4.47
150*150	8.60×10^{-2}	3.59×10^{-2}	245x141	10.4

3.2.2 Slit Aperture

The characteristics of light passes through a square aperture have been studied in 3.2.1. Since many researches have verified the extraordinary transmission could be obtained in two dimensional slit by FDTD computational results, we want to clarify about subwavelength aperture in detail in this section.

First, we reform the square aperture to the slit aperture, the reason why are (a) the previous researches pointed out the localized surface plasmon (LSP) as a critical role in light transmission through subwavelength aperture [11]. Under this condition, the surface structure with better performance is 2-D slit [17]. (b) The previous results showed the different growth tendency of spot size with two orthogonal polarizations. So the 2-D simulation (assumed uniform in Y- (or X-) direction) is not suitable for our case.

Starting our case in the comparison of two square apertures 60*60 (nm^2) and 30*30 (nm^2) by increasing length in Y- direction, silver film was applied for λ=633 nm and the polarization of incidence was in X-,simulation results shown in Fig. 3.2-6.

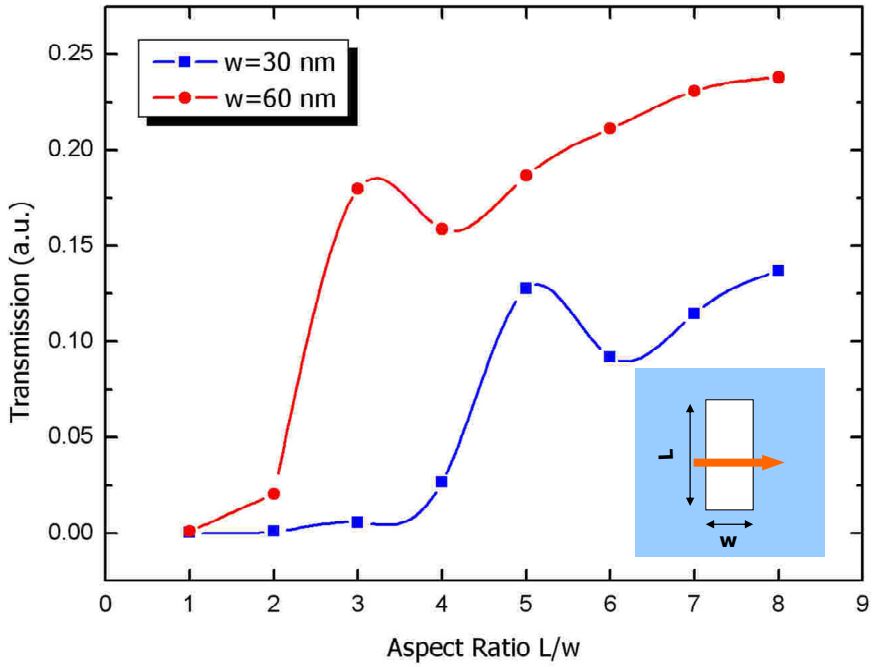

Fig. 3.2-6 Transmission on two slit width (w=30 nm and w=60 nm) varies aspect ratio (AR). The orange arrow means the polarization of incidence is X- (Ex-Hy-Ez exists).

The definition of aspect ratio (AR) is the ratio of length (Y-) to width (X-). That means the aperture is square while AR=1 and slit otherwise, respectively. We limit discussion on AR > 1 and the polarization of incidence in X- direction.

The difference of length between two nearby sides approach specific order (AR=5 for w=30 nm; AR=3 for w=60 nm), while AR is larger than the critical point, the localized surface plasmon (LSP) will dominate transmission.The sudden burst of transmission appears for the slit structure. The field component with AR=1 and 3 for w=60 nm in X- polarization incidence (Ex- Ez- Hy) were shown in Fig 3.2-7. The phenomenon could be observed inside the aperture. The Ex component in square aperture is weak but strong in slit. Since the energy to z was defined by Poynting vector Pz ($E_X \times Hy$), the slit shape could excite stronger localized surface plasmon (LSP) due to the boundary condition and interaction between two side of aperture perpendicular to the polarization.

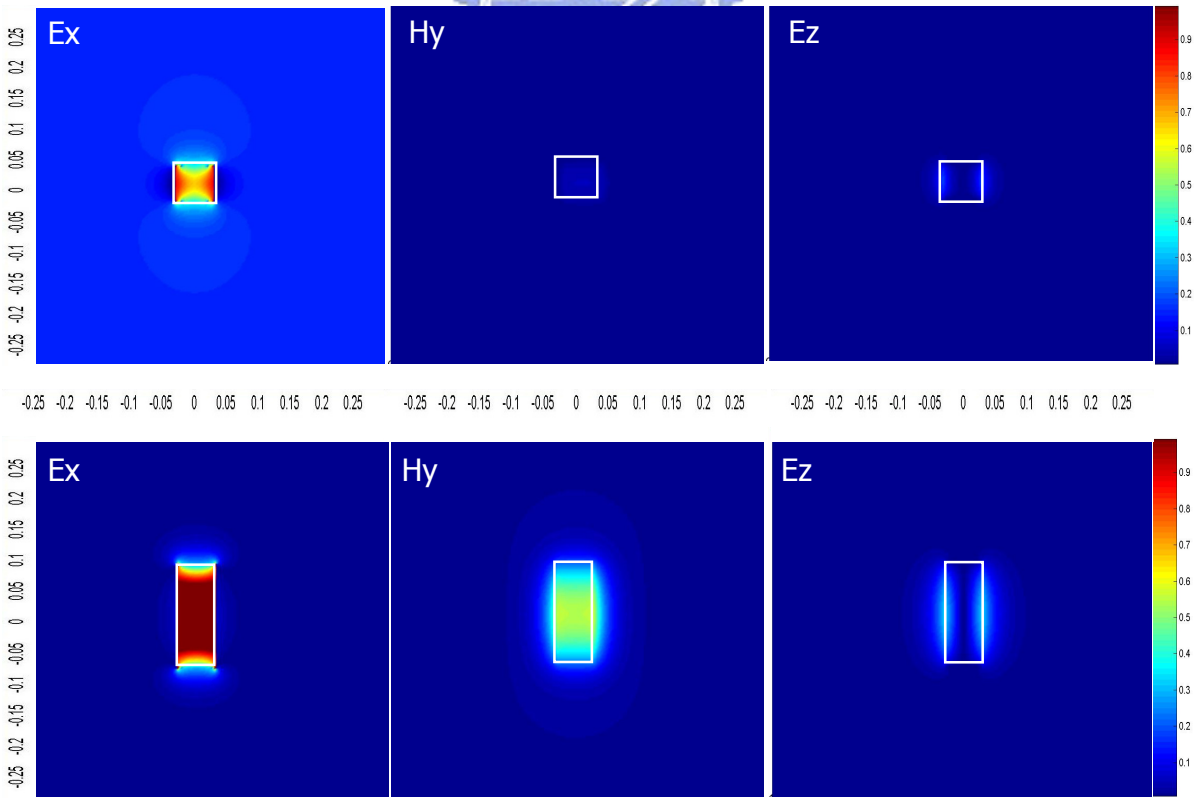

Fig 3.2-7 Plots of field component distribution. The upper is square with side width 60 nm (AR=1), the lower is slit apertures w=60 nm L=180 nm (AR=3).

The Ex-component in the plots above could help us to understand the phenomena occurred at the boundary. At the side perpendicular to the incident polarization (Y-), the Ex exists, and being weaker where close to the parallel side. When the length perpendicular is larger than parallel enough, the strong interaction happened at two long side will be dominant for light transmission mechanism.

Moreover, Fig. 3.2-8 plots the Poynting vector and field distribution, which shows the energy flow clearly again.

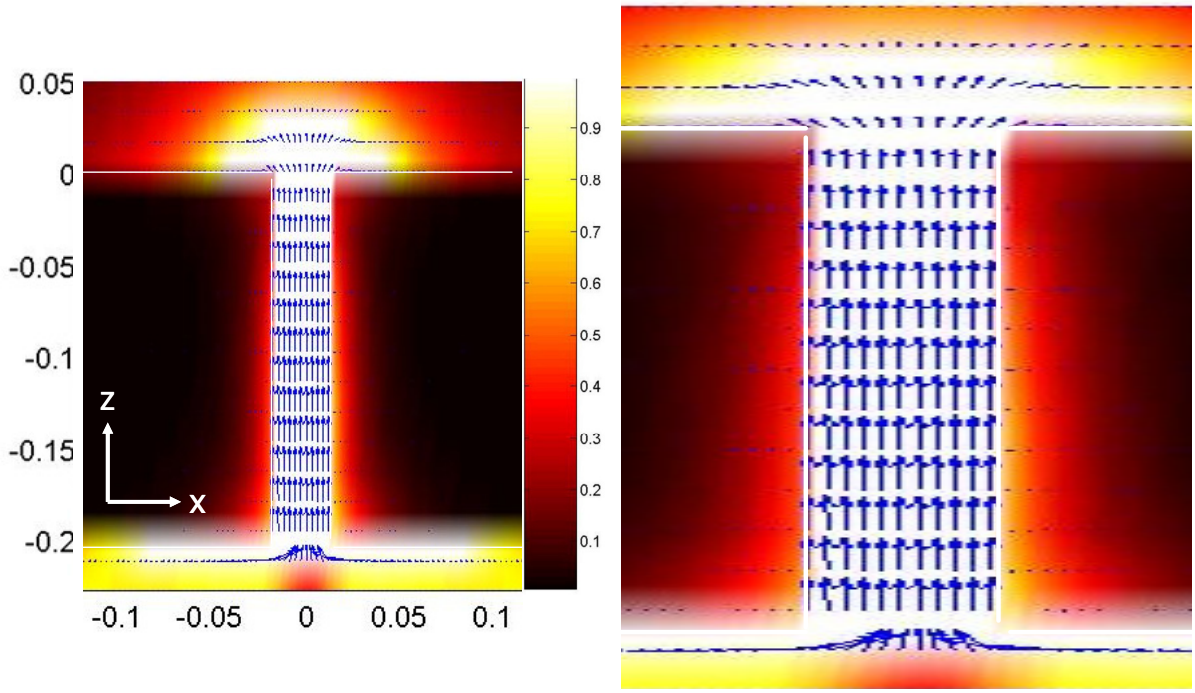

Fig. 3.2-8 Plot of Poynting vector on X-Z plane for slit aperture for w=30 nm and L=150 nm.

Comparing 3.2-8 with 3.2-3, the energy flow of these two plots are totally different. The flow in 3.2-3 decays inside. When incidence passes through the tunnel, the energy has become extremely weak and almost been un-detectable. On the contrary, the Poynting vector strength in 3.2-7 shows the energy inside the slit would not decays until exits the aperture. The observations verify the EM wave could propagate in subwavelength aperture where the propagation mode would even not be sustained. The behavior is explained by localized surface plasmon (LSP) in many

researches. We should also note the decaying while incidence leaves the aperture is the reason why these researches are always been in near-field optics range.

On the other hand, the spot performance was shown in Fig. 3.2-9. Due to the discussions in 3.2.1, the width (X-) of the aperture is fixed in 30 and 60 nm. The spot in X-direction for both two are kept as constants (~123 nm and ~147 nm). In addition, the length (Y-) is increased gradually. The spot size in Y-direction is getting larger linearly.

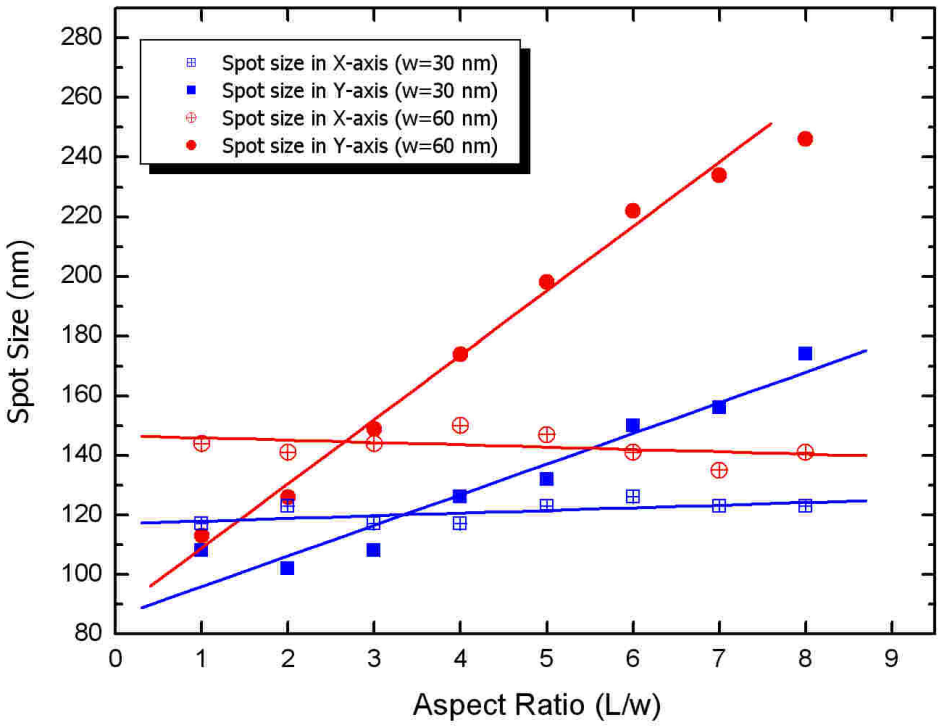

Fig. 3.2-9 Spot size on two slit width (w=30 nm and w=60 nm) varies aspect ratio (AR).

According to the results in section 3.2.1 providing that the spot size is restricted by geometric structure. And the smaller spot and the higher transmission is the top priority for the demand. Utilizing the parameter introducing before, power throughput density (PTD) helps to recognize the slit aperture. An aperture with higher PTD value may be the first choice in our request. As shown in Fig. 3.2-10. The maxima PTD value is occurred at w=30 nm and L=150 nm. PTD reaches to ~130. The

result reveals the thinner width of aperture may bring high optical efficiency with dual application in transmission and spot size.

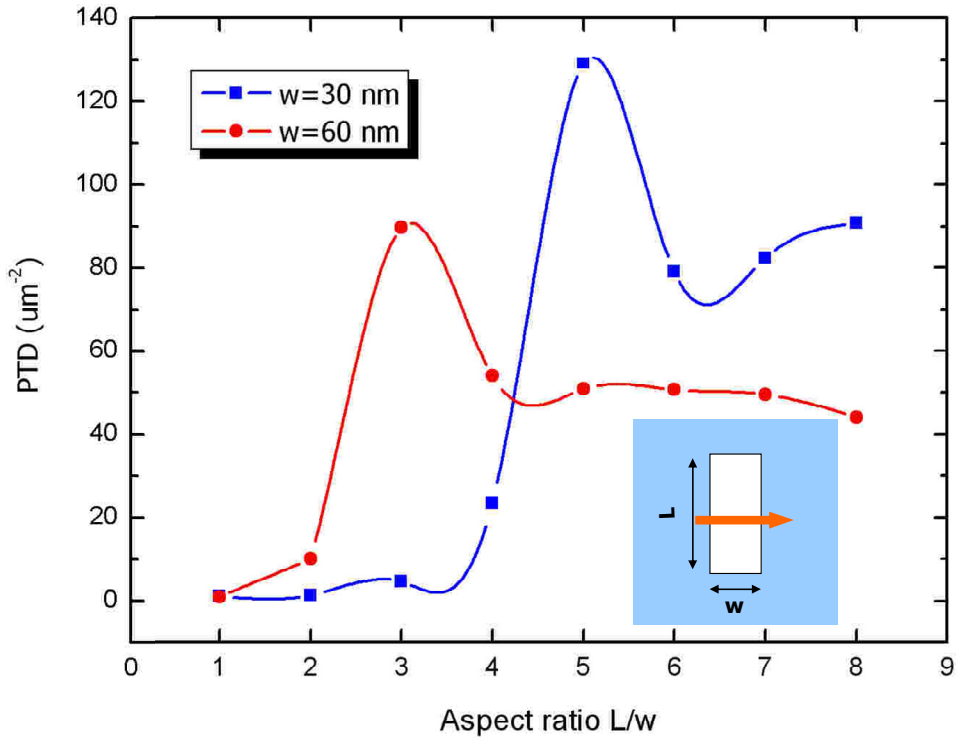

Fig. 3.2-10 Transmission on two slit width (w=30 nm and w=60 nm) varies aspect ratio (AR). The orange arrow means the polarization of incidence is X- (Ex-Hy-Ez exists).

3.2.3 Ridge-based Aperture

Since many researches aim for producing the spot with higher power and smaller size beyond diffraction limit. The triangle or I- shaped (or H-shaped) apertures had been applied. The most important and effective structure is the C-shaped aperture designed by Hesselink *et al.* Most of us believe that some special mechanisms bringing great transmission are happened while light get through the aperture. And these effects would not be occurred in circular or square aperture. We are curious about them. The simulations following and discussions might help us to distinguish and realize some characteristics of them.

We first introduced C-shaped aperture with the optimized parameter at thickness is 200 nm for silver film and λ=633 nm [28]. The C-aperture and I-aperture could be viewed as morphing design by adding the arms, as shown in Fig. 3.2-11. (a) slit-, (b) C- and (c) I- shaped are the apertures morphing from a slit. To note that the cut-off wavelength of the fundamental propagation mode is at 420 nm, 577 nm and 600 nm for slit-, C-, and H-shaped aperture, respectively [29]. The wavelength of incidence is 633 nm. Under the condition, no propagation mode could be sustained in such structures.

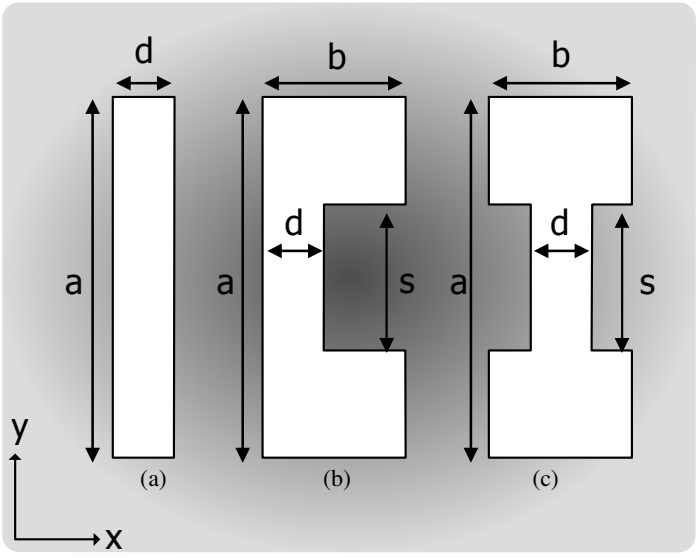

Fig. 3.2-11 The structures of (a) slit-, (b) C-, and (c) I-aperture, the length parameters are corresponding to a=210 nm, b=84 nm, d=38 nm, and s=86 nm.

In the simulations, the slit's direction was along the y-axis, as depicted in Fig. 3.2-12. Since the slit is asymmetrical in two directions X- and Y-, the PT is highly dependent on the incident polarization. Then we made an observation at a plane of 50 nm from the exit plane of the aperture and estimated the FWHM (Full Width at Half Maximum) as the spot size. In addition, the thickness of metal plate was modulated to perform strong coupling of localized surface plasmon (LSP) distributed over metallic layer, and discuss the contribution of high PT from LSP effect.

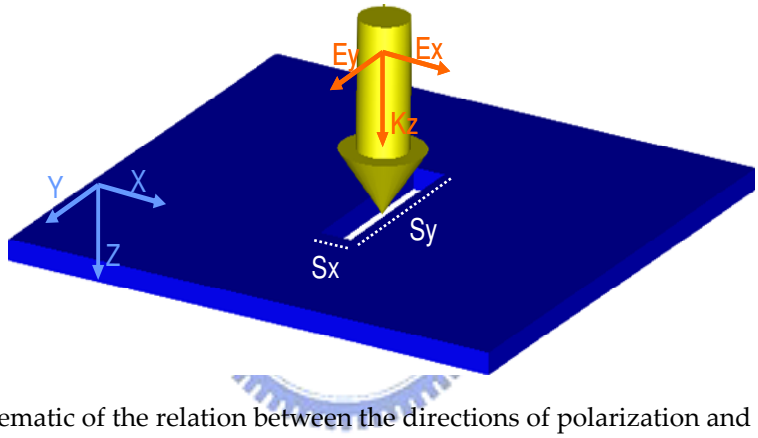

Fig. 3.2-12 Schematic of the relation between the directions of polarization and the ridge.

The apertures were made on silver plate (n=0.14+4.00i for λ=633 nm) with thickness of 200 nm were illuminated by x- and y-polarized light, respectively. The spatial distributions of the electric field were depicted in Fig. 3.2-11, where (a)-(c) illustrating C-, slit- and I-shaped apertures under x-polarized incidence and (d)-(f) under y-polarized incidence. The surface plasmon polariton was induced by the incident x-polarized illumination, and hence increasing photon capturing capability through the aperture. The transmission power from x-polarization is much larger than y-polarization on the order of 10^3 times. Under the boundary condition inside the slit, E_y, i.e., the E-field parallel to the slit should be zero at the two edges of the slit, so the transmission is weak, as shown in Fig. 3.2-13 (d)-(f). In contrast, when x-polarization illuminated onto the silt, yielding to the same boundary condition, E_x,

i.e., the E-field perpendicular to the slit exists at the two edge of the slit. Furthermore, the z component of Poynting vector, P_z, is defined by $E_x \times H_y$, dominating the propagating characteristics. Thereby, the transmission of x-polarized light is stronger than y-polarization. The field distributions of every component corresponding to two orthogonal polarization incidence on slit (w=38 nm) was shown in Fig. 3.2-14 and 15 In the same way, only x-polarization responds to PT of C-aperture. This indicates C-aperture or slit follows the same mechanism, i.e., LSP; moreover, the dominant geomorphic factor should be the ridge.

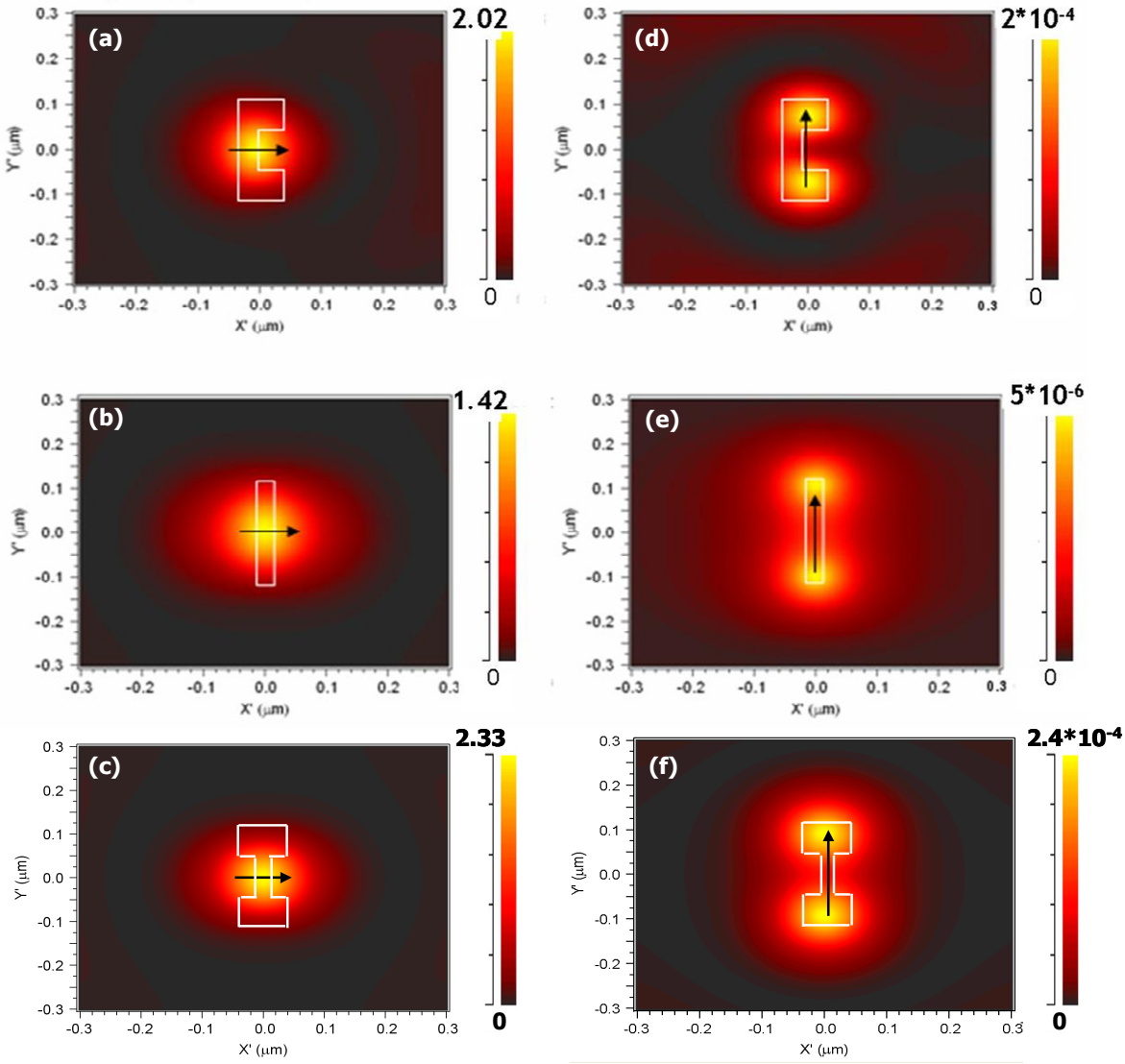

Fig. 3.2-13 $|E|^2$ distributions at 50 nm from the exit plane of the apertures. (a), (b) and (c) C-, slit- and I- aperture with x-polarization incidence; and (d), (e) and (f) with y-polarization incidence.

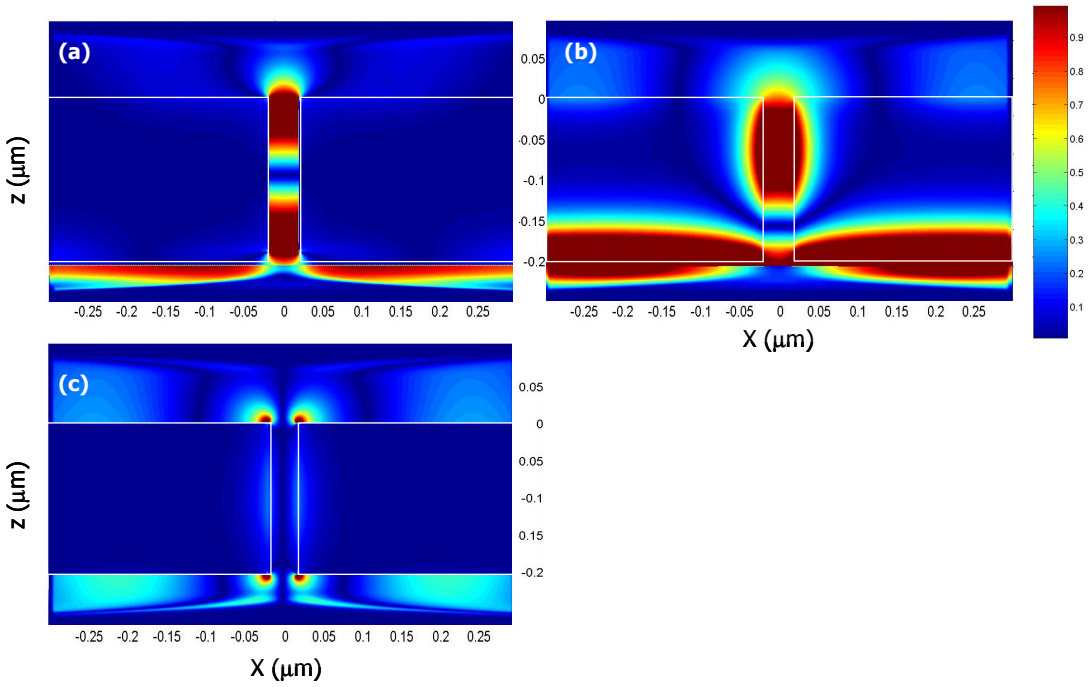

Fig. 3.2-14 Plots of (a)Ex ,(b) Hy and (c) Ez for the case of X- illumination.

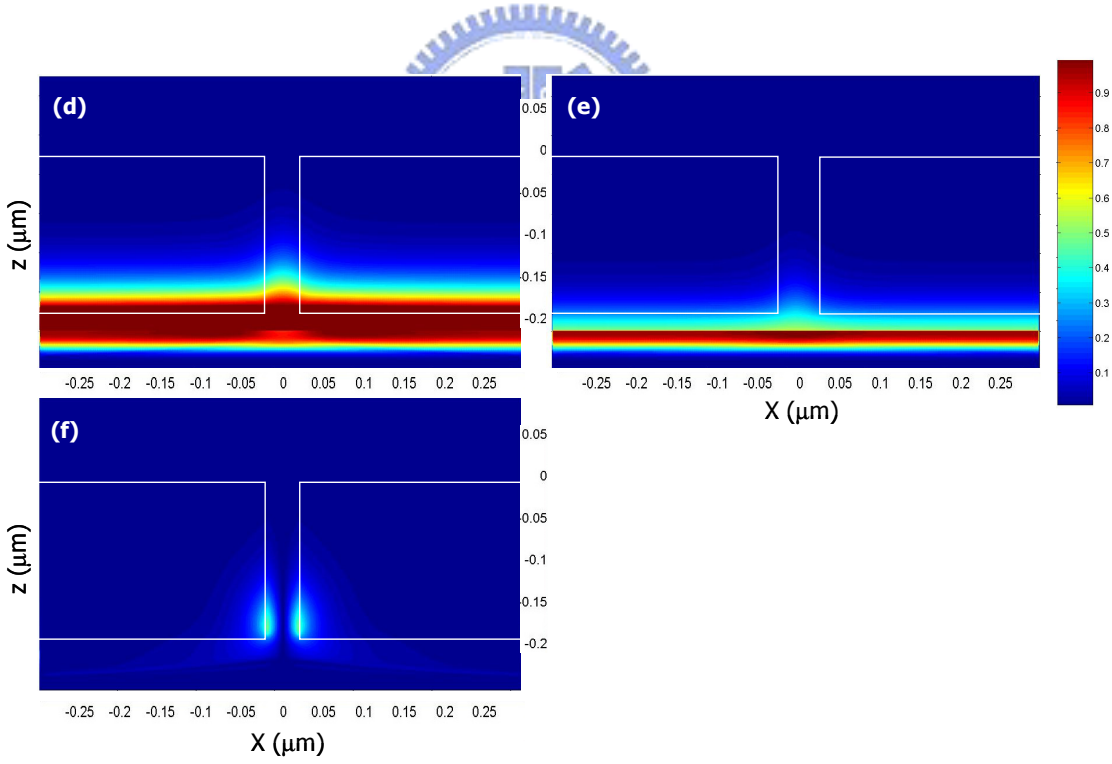

Fig. 3.2-15 Plots of (d) Hx, (e) Ey and (f) Hz for the case of Y- illumination.

Moreover, PTs from various apertures are shown in Table 3.2-2. C and I-shaped exhibits a close value of power throughput. We inferred that the slit of both apertures supports the similar PT enhancement from LSP, no matter the overall shape is C or I. On the contrary, single slit exhibits a higher PT = 1.3, accompanying an asymmetrically expanding spot size.

In the preceding discussion, slit made a suitable geometry of electromagnetic boundary condition for LSP resonance. Meanwhile, C- and I-aperture could be viewed as an expanded slit shape and lead to smaller SPR effect and divergence.

Table. 3.2-2 Comparisons of PT and spot size of slit-, C- and I-shaped aperture.
i.e., the "area" is the aperture physical area.

Aperture	Area (λ^2)	PT (a.u.)	Spot size (nm^2)	PTD (μm^{-2})
Slit	0.02	1.30	126x156	66.1
C	0.032	1.27	118x128	89.5
I	0.032	1.27	118x128	89.5

The transmission of the subwavelength aperture can be further investigated by the thickness of the metallic film. For x-polarized illumination, we found the PT oscillating with the aperture depth, as shown in Fig. 3.2-16(a). The first two peaks of the C-aperture were located at 200 nm and 475 nm and I-aperture were located at 225 nm and 500 nm respectively. For different depths of single silt, PT was globally higher than that of C-aperture, especially at 250 nm and 600 nm. Physically, the depth 300 nm was near the half of incident wavelength 633 nm, which was the resonance condition inside the rectangular cavity. PT enhancement factor was affected by the depth as well as the slit shape. The phenomenon of the enhancement inside the subwavelength aperture was the resonance effect. The slit plays the primary role of light enhancement neither C-aperture nor I-aperture morphing from

slit which was consistent with the expectation of LSP characteristic.

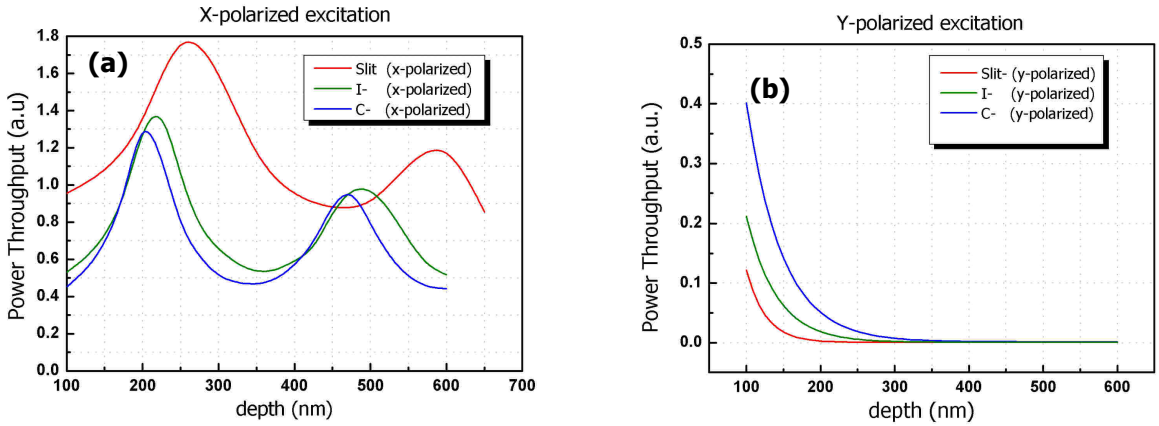

Fig. 3.2-16 Power throughput comparison of slit-, C- and I- aperture versus the depth of aperture under (a) x- and (b)y-polarized illumination.

We also observe the resonance modes exist the aperture through the Poynting vector chart and energy distribution, as shown in Fig. 3.2-17.

Furthermore, the results in Fig. 3.2-16(b) demonstrated that the PT excited by y-polarization exponentially decays in both structures. Slit aperture decays sharper than C- and I-aperture under the cut-off condition. The slit-shaped aperture is more sensitive than C-shaped aperture with two polarization incidence, because the arms of C-, I-aperture would make y-polarized light inducing LSP effect. We could observe that PT in slit- is generally higher than C- and I-aperture in x-polarized excitation, as shown in Fig. 3.2-16(a), but lower in y-polarized excitation, as shown in Fig. 3.2-16(b).

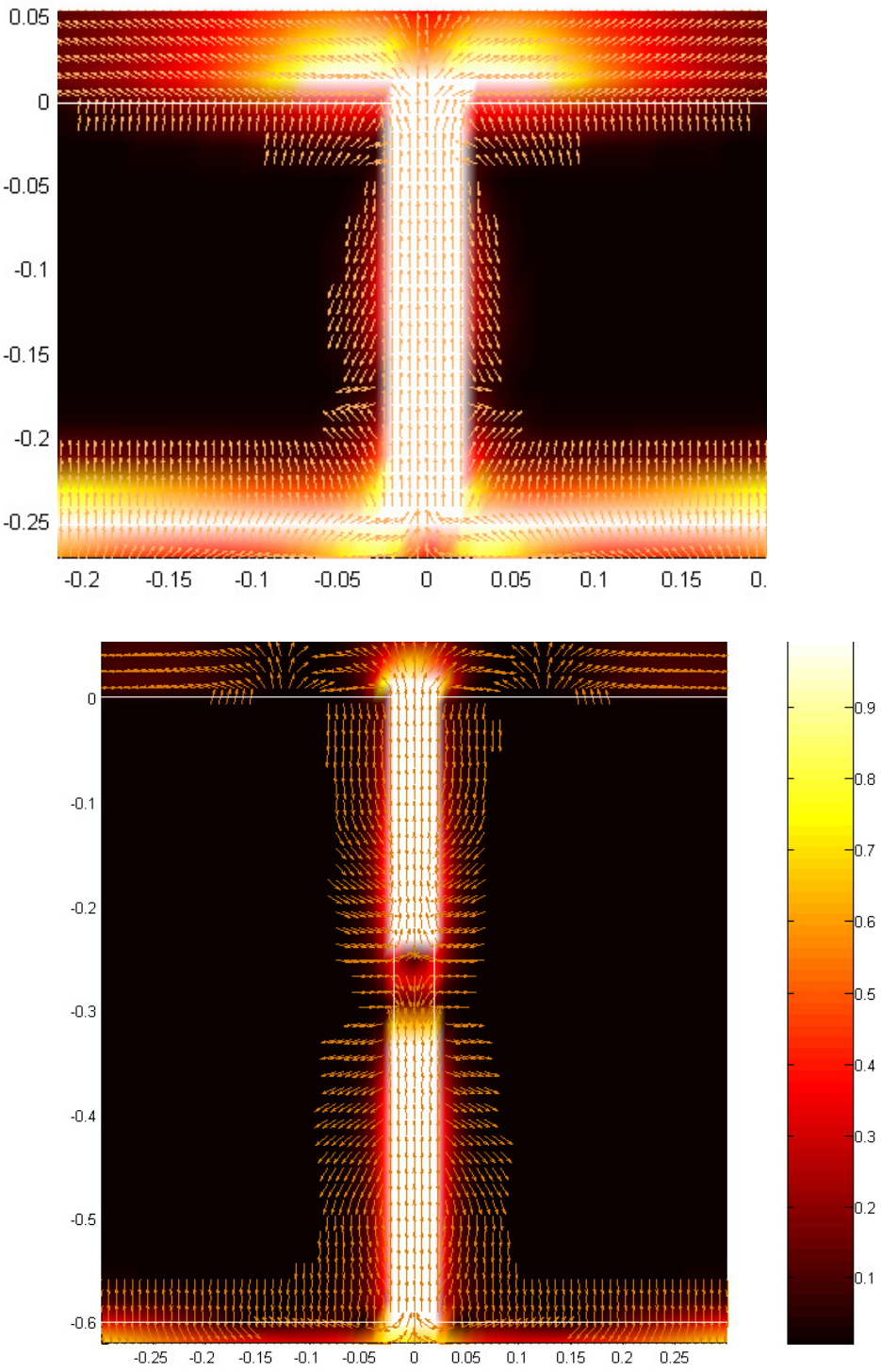

Fig. 3.2-17 Plot of Poynting vector on X-Z plane for slit aperture for w=38 nm and L=2100 nm with thickness=250 (upper) and 600 nm (lower).

Allowing the coupling condition of LSP, the x-polarized light showed much stronger transmission than y-polarization. Furthermore, since the PT for the x-polarization is owed to the cavity behavior of LSP, It indicates that power throughput enhancement can be achieved by optimizing the depth of nano-apertures. According to the results, slit-, C- or I-aperture follows the same photon capture mechanism- SPR; In other words, the dominant geomorphic factor should be the ridge, i.e., the slit. Fig. 3.2-18, the field component distribution in X-polarization incidence reveals the similar light transmission mechanism.

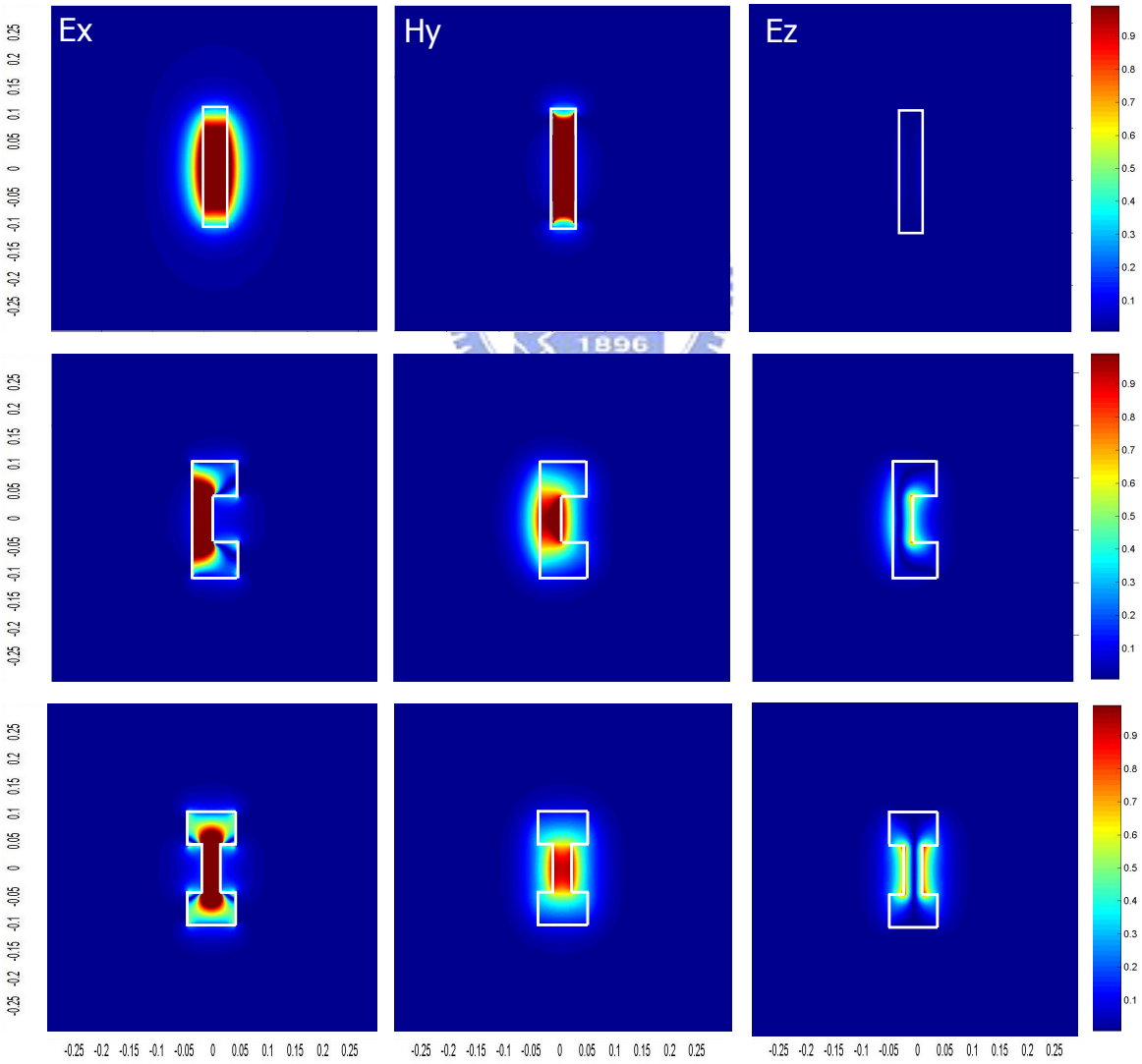

Fig. 3.2-18 Plots of field components in X-Y plane for three kinds of apertures (Ex, Hy and Ez corresponds to left, middle and right column, respectively).

In Section 3.2, the mechanisms of great transmission for special subwavelength apertures were studied. The simulation results show also the trade-off between high transmission and spot beyond diffraction limit might be solved by employing localized surface plasmon (LSP). At the last, the particular phenomenon attracts our attention. Since the slit aperture with high symmetric to match the specific linear-polarization incidence (X-polarized in our case), the C-shaped aperture due to its non-symmetrical boundary condition could make the spot size smaller. We try to combine these two merits in our design.

3.3 Composite Structure

According to the previous discussion, the slit made a suitable geometry of electromagnetic boundary condition for LSP effect. On the other hand, the C-aperture could hold a smaller spot size. Taking both advantages of slit and C-aperture, we proposed a new composite structure shown in Fig 4.1-1. At the incidence plane on a metallic thin film, it is a slit-aperture, and at the exit side, it is a C-aperture. Alternatively, the structure can be viewed as a slit but with two "arm-grooves" at the exit side.

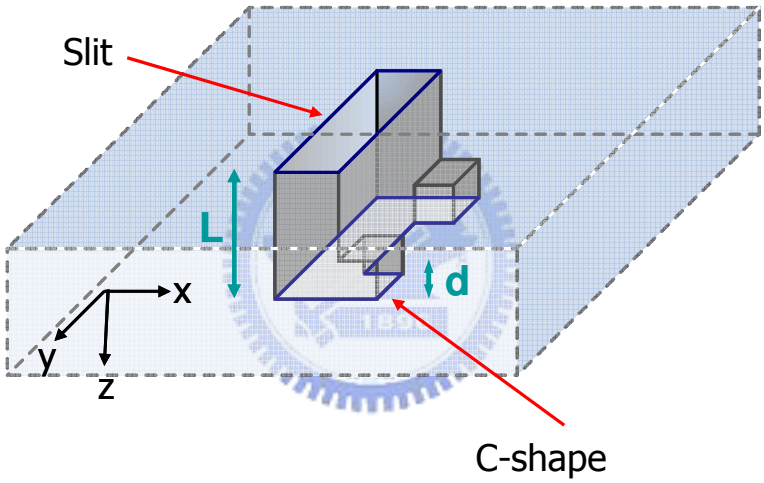

Fig. 3.3-1 Schematic diagram of the composite structure with parameters, L and d.

The shapes of apertures on the both sides follow the same design as in the preceding discussion (Fig3.2-9). In the simulation model, we modulated different the depths of the slit, L, and the depths of the arm-grooves, d. The PT and spot size of different parameters were shown in Fig. 3.3-2

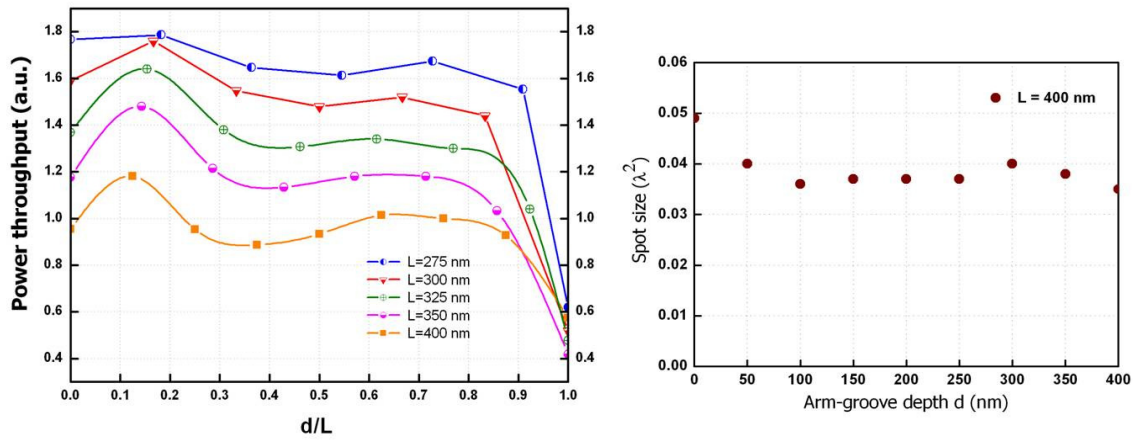

Fig. 3.3-2 The dependence of PT on arm-grooves depth d (left). And, the spot size is nearly the same as the case of a C-aperture (right).

The parameter d/L means the aperture is a pure slit while d/L=0 (or say d=0) and is pure C-shaped aperture while d/L=1 (or say d=L). Otherwise, it is a composite aperture we proposed.

At the same time, the composite structure with dual slit- and I- aperture was proposed for comparison, as shown in Fig. 3.3-3, 4.

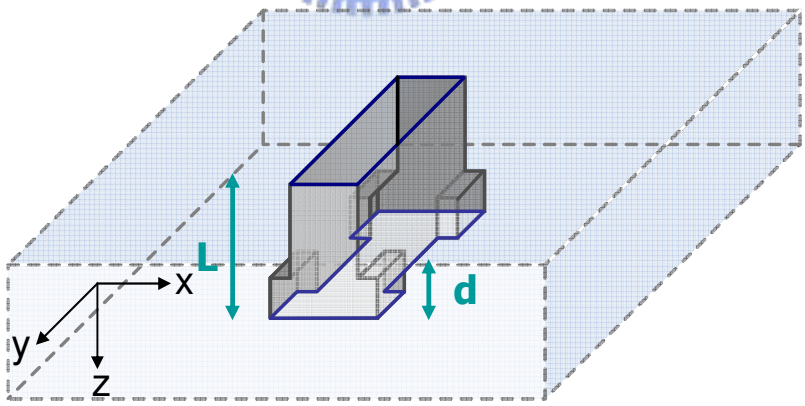

Fig. 3.3-3 Schematic diagram of the composite structure with slit- and I-aperture.

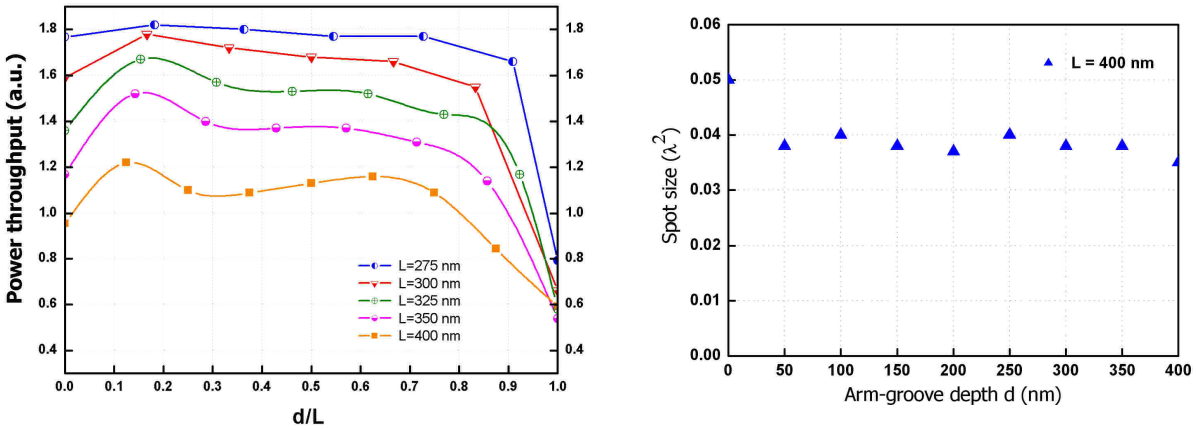

Fig. 3.3-4 The dependence of PT on arm-grooves depth d (left). And, the spot size is nearly the same as the case of an I-aperture (right).

The result reveals PT is similar to a pure slit. Meanwhile, spot size performance is the same as the C-shaped (or I-shaped) aperture, which is smaller compared with a pure slit. We also have an idea that the changed boundary at the entrance plane might affect the transmission but could not reform the spot size (or field distribution). On the contrary, the changed boundary at the exit plane will reform the spot performance directly. We should note if we change the boundary at exit plane only, it also will influence the transmitted power due to the resonance modes existence inside the aperture. We finally simulate the condition to prove our thought. For (a) pure slit- aperture, (b) pure C-aperture, (c) slit – C composite structure, and (d) C – slit composite aperture. All the parameter include width, length, material, incidence were like we discussed before, thickness is 400 nm and arm groove depth is 100 nm. As shown in Fig. 3.3-5, and the simulation result was shown in Table. 3.3-1.

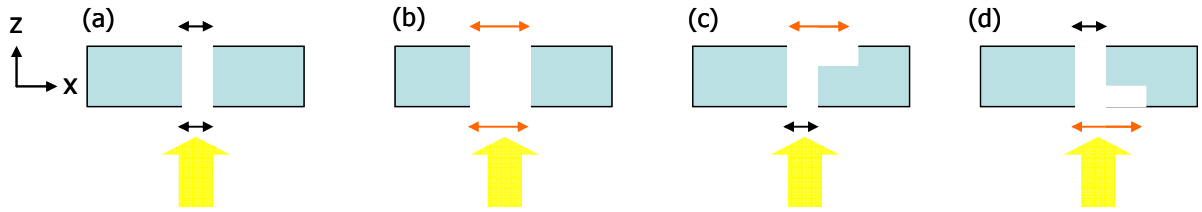

Fig 3.3-5 Schematic diagrams of four different apertures, (a) slit at both side, (b) C-aperture at both side, (c) slit at entrance and C- at exit side, and (d) C-at entrance and slit at exit side.

Table 3.3-1 Comparisons of the aperture in Fig 3.3-5

(RPTs was PTs were normalized to the PT of slit)

Aperture	(a) Slit	(b) C	(c) Slit-C	(d) C-Slit
*RPT (a.u)	1	0.597	0.990	0.743
Spot Size (nm^2)	126x156	118x128	120x132	130x150
*RPTD	1	0.776	1.23	0.75

It was demonstrated the transmission mechanism of a nano-aperture can be conceptually divided into three parts: (a) "photon capture" at the entrance plane (b) cavity resonance mode along the edge walls, and (c) "spot performance" at the exit plane, as shown in Fig. 3.3-6.

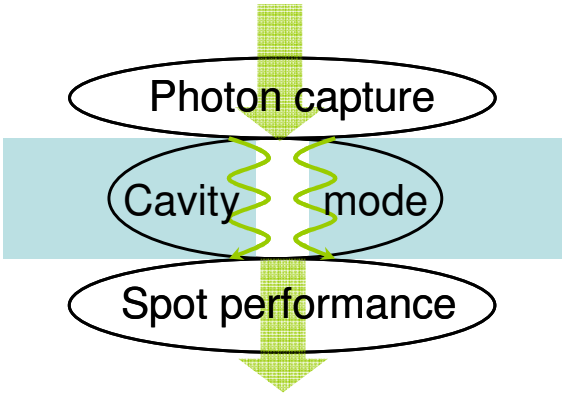

Fig. 3.3-6 Conceptual scheme of LSP-assisted transmission mechanism which triggered the design of composite structure.

The mechanism of high transmission throughput of nano-aperture has been suggested by localized surface plasmon effect and the cavity resonance inside the aperture. The results in 3D FDTD simulation showed that the shape design of an aperture at exit plane plays a crucial role as spot size performance. Therefore, a new composite structure of aperture with slit-form at the incident plane and C-form at the exit plane has been demonstrated. Compared to the proposed optimal performance of a C-aperture, the new design shows a higher PT and unchanged spot size.

Chapter 4 Conclusion and Future Work

4.1 Conclusion

The relation between mechanism of extraordinary high transmission through a subwavelength aperture and localized surface plasmon (LSP) has been study in this thesis. We verified that the gap determined the transmitted power and the spot size principally and the simulation results also show the polarization dependence might be explained by boundary condition of electric-magnetic field theory. That means it should be the cardinal principle concerned first while the aperture was downsized to subwavelength scale. Meanwhile, the power throughput density (PTD) efficiency of conversional square aperture ($30*30\text{-nm}^2$) could be enhanced to 187X by modifying the aperture shape become slit ($30*150\text{-nm}^2$). The crucial role played by localized surface plasmon (LSP) dominated the great transmission and kept the spot size at the similar scale ($\sim 0.2*0.2\lambda^2$) due to its geometric dimension.

Base on the conclusions above, we also clarified the physical mechanism which leads to unusual transmission through the C-, I-aperture were the same to slit-aperture. The results described the shape of the aperture was not the first priority we concerned about. Exactly, the first we should note is the width and length of gap. The stronger localized surface plasmon will be excited while the gap is thinner, and the length of gap could influence the magnitude of transmitted power.

An innovative composite structure was proposed and successfully demonstrated by simulations. The combination of the slit- and the C-aperture, which signifies the hybrid of the localized surface plasmon coupling effect, stands for a dual applicability in data storage system and biosensor engineering.

Such a nano-aperture design transcends over the conventional concept and extends its feasibility to another applied technology.

We finally make the conclusion to take the mechanisms of transmission through subwavelength apart into three parts: (a) "photon capture" at the entrance plane (b) cavity resonance modes along the edge walls, and (c) "spot performance" at the exit plane. On the other words, if we define the function: G_{in} $(\lambda, g_{in}(\lambda,w))$, $R(\lambda, t)$, and G_{out} $(\lambda, g_{out}(\lambda,w))$, where G is geometric factor, λ is wavelength of incidence, g is gap width factor, w is gap width, R is resonance modes existence factor, t is thickness of aperture and subscript in or out means at entrance or exit plane. Then the transmitted power T is defined as $T(\lambda,w,t) = G_{in}(\lambda, g_{in}(\lambda,w)) \times R(\lambda, t) \times G_{out}(\lambda, g_{out}(\lambda,w))$. Moreover, the spot size performance S is defined as $S(\lambda,w) = G_{out}(\lambda, g_{out}(\lambda,w))$. This conclusion will help us to analyze the topic of subwavelength aperture clearly and avoid concerning all the effects at the same time.

4.2 Future Work

Although the simulations provide the arguments we done, the experiment is needed to support them. The subwavelength aperture with gap width about 50 nm could be achieved by focus ion beam (FIB) process. And the near-field measurement is enabled by near field scanning optical microscope (NSOM) system. On the other hand, this thesis focuses on only a subwavelength aperture, according to the study by T. Ebbesen *et al.* The trench structure is another crucial role on high transmission through a subwavelength aperture. To combine these characteristics, optimization of it will be possible.

Reference

[1] H. A. Bethe, "Theory of diffraction by small holes", *Phys. Rev*. 66, 163-182 (1944).

[2] T. W. Ebbesen, H.J. Lezec, H.F. Ghaemi, T. Thio & P.A. Wolff, "Extraordinary optical transmission through sub-wavelength hole arrays", *Nature* 391, 667-669 (1998).

[3] H. F. Ghaemi, T. Thio, D. E. Grupp, T. W. Ebbesen and H. Lezec, "Surface plasmons enhance optical transmission through subwavelength holes", *Phys. Rev. B* 58, 6779-6782 (1998).

[4] T. Thio, J. J. Lezec, and T. W. Ebbesen, "Strongly enhanced optical transmission through subwavelength holes in metal films", *Phycia B* 279, 90 (2000)

[5] T. Thio, K. M. Pellerin, R. A. L inke, H. J. Lezec and T. W. Ebbesen, "Enhanced optical transmission through a single subwavelength aperture," *Opt. Lett.* Vol. 26, P. 1972 (2001)

[6] T. Thio, J. J. Lezec, T. W. Ebbesen, K. M. Pellerin, G. D. Lewen, A. Nahata, and R. A. Linke,"Giant optical transmission of subwavelength apertures: Physics and applications", *Nanotechnology* 13, 429 (2002)

[7] H. J. Lezec, A. Degiron, E. Devaux, R. A. Linke, L. Martìn-Moreno, F. J. Garcìa-Vidal, and T. W. Ebbesen, "Beaming light from a subwavelength aperture", *Science* 297, 820 (2002)

[8] William L. Barnes Alain Dereux & Thomas W. Ebbesen,"Surface plasmon subwavelength optics", *Nature* (2003).

[9] F. J. Garcìa-Vidal, H. J. Lezec, T.W. Ebbesen, and L. Martìn-Moreno, "Multiple paths to enhance optical transmission through a single subwavelength slit", *Phys. Rev. Lett.* 90(21), 213901(2003)

[10] A. Degiron and T. W. Ebbesen, “Analysis of the transmssion process through single aperture surrounded by periodic corrugations”, *Opt. Exp*. 12(16), p. 3694-3700 (2004)

[11] A. Degiron, H.J. Lezec, N. Yamamoto, T.W. Ebbesen, ”Optical transmission properties of a single

subwavelength aperture in a real metal”, *Opt. Commun*.239 (2004) 61-66.

[12] H. Raether, “*Surface Plasmons on Smooth and Rough Surfaces and on Gratings”*,(Springer-Verlag,Berlin,1988).

[13] J. D. Jackson, “Classical Electrodynamics”, 3rd edition, Wiley, New York, 1999.

[14] Tuomas Vallius, Jari Turunen ,Masud Mansuripur and Seppo Honkanen,” Transmission through single subwavelength aperture in thin metal films and effects of surface plasmons”, *. J. Opt. Soc. Am. A*/Vol. 21, 2004

[15] Y. Xie, A. R. Zakharian, J. V. Moloney, and M. Mansuripur, "Transmission of light through periodic arrays of sub-wavelength slits in metallic hosts", *Opt. Express* **14**, 6400-6413 (2006).

[16] A. R. Zakharian, J. V. Moloney, and M. Mansuripur,“Surface plasmon polaritons on metallic surfaces”,*Opt. Express.* 15, 183-197 (2007)

[17] Y. Xie, A. R. Zakharian, J. V. Moloney, and M. Mansuripur, "Transmission of light through slit apertures in metallic films," *Opt. Express* **12**, 6106-6121 (2004),

[18] K. Tanaka, T. Ohkubo, M. Oumi, Y. Mitsuoka, K. Nakajima, H, Hosaka, and K. Itao, ”Numerical simulation on read-out characteristics of the planar aperture-mounted head with a minute scatterer,” *Jpn. J. Appl. Phys*., Vol. 40, P. 1542 (2001)

[19] K. Tanaka, M. Oumi, T. Niwa, S. Ichihara, Y. Mitsuoka, K. Nakajima, T. Ohkubo, H. Hosaka and K. Itao, "High Spatial Resolution and Throughput Potential of an Optical Head with a Triangular Aperture for Near-Field Optical Data Storage," *Jpn. J. Appl. Phys*., Vol 42, P. 1113 (2003)

[20] K. Tanaka and M. Tanaka, "Optimized computer-aided design of I-shaped subwavelength aperture for high intensity and small spot size," *Opt. Commun*.. Vol. 233, P. 231 (2004)

[21] X. Shi, L. Hesselink, and R. L. Thornton, "Ultrahigh light transmission through a C-shaped nanoaperture," *Opt. Lett*.. Vol. 28, No.15, P. 1320 (2003) - 93 -

[22] K. S. Yee,"Numerical solution of initial boundary value problems involving Maxwell'sequationsin isotropic media," *IEEE Trans. Ant. Prop.* **14**, 302-307, 1966.

[23] A. Taflove, and S. C. Hagness, "Computational electrodynamics: The Finite-Difference Time-Domain method 2nd Ed," *Artech House Publishers*, Boston, 2000.

[24] K. S. Kunz and R. J. Luebbers, The Finite Difference Time Domain Method for Electromagnetics, Boca Raton, CRC Press (1993)

[25] A. Taflove, *Advances in Computational Electrodynamics*, Boston, Artech House (2001)

[26] P. Drude, *Ann. Phys., Lpz.* **1** 566 (1900)

[27] E. D. Palik, "Handbook of optical constants of solids", New York: Academic Press (1985)

[28] Yu-Chien Chen, Jen-Yu Fang, Chung-Hao Tien, and Han-Ping D. Shieh High-transmission hybrid effect assisted nanoaperture, *Opt. Lett*. 31, 655 (2006)

[29] J. Helszajn: Ridge waveguides and passive microwave components (IEE, London, 2000) p. 26